

A phase I/II trial of WT1-specific TCR gene therapy for patients with acute myeloid leukemia and active disease post-allogeneic hematopoietic cell transplantation: skewing towards NK-like phenotype impairs T cell function and persistence

Received: 31 March 2025

Accepted: 21 May 2025

Published online: 05 June 2025

 Check for updates

A list of authors and their affiliations appears at the end of the paper

Relapsed and/or refractory acute myeloid leukemia (AML) post-allogeneic hematopoietic cell transplantation (HCT) is usually fatal. We previously reported that post-HCT immunotherapy with Epstein-Barr virus (EBV)-specific donor CD8⁺ T cells engineered to express a Wilms Tumor Antigen 1-specific T-cell receptor (T_{TCR-C4}) appeared to prevent relapse in high-risk patients. In this phase I/II clinical trial (NCT01640301), we evaluated safety (primary endpoint), persistence and efficacy (secondary endpoints) of EBV- or Cytomegalovirus (CMV)-specific T_{TCR-C4} in fifteen patients with active AML post-HCT. Infusions were well tolerated, with no dose-limiting toxicities or serious adverse events related to the product. However, T_{TCR-C4} cells did not clearly improve outcomes despite EBV-specific T_{TCR-C4} cells showing enhanced potential for prolonged persistence compared to CMV-specific T_{TCR-C4}. Investigating the fate of persisting T_{TCR-C4}, we identified a shift towards natural killer-like (NKL) terminal differentiation, distinct from solid tumor-associated canonical exhaustion programs. In one patient, treatment with azacitidine appeared to mitigate this NKL skewing, promoting T_{TCR-C4} persistence. These findings suggest that AML drives a distinct form of T-cell dysfunction, highlight the need for targeted approaches that preserve T-cell fitness, ultimately improving the efficacy of cellular therapies for AML.

Relapsed/refractory acute myeloid leukemia (AML) after allogeneic hematopoietic cell transplantation (HCT) poses a major therapeutic challenge^{1,2}, with a 2-year overall survival (OS) rate below 20% and only 4% if relapse occurs within six months post-HCT¹⁻³. Salvage therapies, including intensive chemotherapy, donor lymphocyte infusions (DLI), and second HCTs have shown limited efficacy, underscoring the urgent need for novel therapies.

Pioneering trials⁴⁻⁷ have demonstrated that adoptive T-cell therapy targeting Epstein-Barr virus (EBV) or cytomegalovirus (CMV) effectively

treats post-transplant lymphoproliferative disease, thereby establishing antigen-specific T-cell therapies as a viable approach post-transplant. Building on this foundation, various efforts have sought to extend cell therapy to target tumors. The Wilms' Tumor 1 (WT1) protein is an attractive AML immunotherapy target⁸, as WT1 overexpression promotes proliferation and oncogenicity⁹⁻¹¹. In a phase I/II trial, targeting WT1 in the post-HCT setting, we genetically modified matched donor CD8⁺ T cells to express a high-affinity WT1-specific T-cell receptor (TCR_{C4}) specific for the HLA-A*0201-restricted WT1₁₂₆₋₁₃₄ epitope. To

 e-mail: achapuis@fredhutch.org

minimize the potential for graft-versus-host disease (GVHD) mediated by infused donor cells¹², EBV-specific or CMV-specific CD8⁺ T cells were transduced (T_{TCR-C4}). Prophylactic infusion of EBV-specific T_{TCR-C4} in patients without detectable disease, but at high relapse risk post-transplant (Arm 1), yielded 100% relapse-free survival in 12 patients at a median follow-up of 44 months¹³. Although the trial was not randomized, this strategy showed an advantage when compared to historical controls who did not receive the same treatment. However, in 15 patients with prior evidence of disease post-HCT discussed here, infused EBV-specific or CMV-specific T_{TCR-C4} did not yield a superior overall survival compared to historical controls^{1,2,14,15}.

The persistence of functional antigen-specific T cells is required for sustained immunotherapy efficacy^{16–18}. In solid tumors and lymphomas, reduced persistence generally correlates with T-cell exhaustion^{16,19}, characterized by markers like PD-1, CTLA-4, Tim3, LAG-3, BTLA and/or TIGIT²⁰. Targeting these immune-inhibitory receptors with checkpoint-blocking antibodies mitigates exhaustion^{21,22}. In AML, recent studies have questioned the presence of T-cell exhaustion²³, proposing alternative mechanisms of immune dysfunction^{24,25}. Natural killer-like (NKL) markers expressed on CD8⁺ T cells have correlated with adverse outcomes, suggesting that NKL skewing may contribute to T-cell dysfunction^{24–26}. However, whether AML directly induces terminally differentiated, dysfunctional antigen-specific T cells remains unclear²⁷.

Understanding the mechanisms of dysfunction that are operative in AML is critical for designing strategies to overcome the current limitations observed in T-cell therapies. Here, we leveraged adoptive transfer of T_{TCR-C4} in refractory or relapsed AML patients to track AML-specific T cells, elucidate AML-induced T cell states, identify the mechanisms responsible for T-cell dysfunction, and inform the design of effective anti-AML therapies.

Results

T_{TCR-C4} is safe, well tolerated, and produces comparable outcomes to conventional treatments for high-risk relapsed/refractory AML patients post-HCT

From April 2013 through February 2019, 15 HLA-A2-expressing patients with relapsed and/or refractory AML post-HCT were enrolled on trial

NCT01640301 (Table 1, and Supplementary Fig. 1). The median age at diagnosis was 40. Pre-HCT, 27% of patients had secondary or treatment-related AML, at diagnosis 47% were adverse risk, and 53% favorable/intermediate risk per European LeukemiaNet (ELN) stratification (Supplementary Table 1)²⁸. Post-HCT, four patients had measurable residual disease (MRD) by -28 days (refractory), two relapsed by 3 months, and nine relapsed after day 100. The median time to relapse was 496 days post-HCT. Thirteen patients received salvage therapy before T_{TCR-C4}, including six who underwent a second HCT. Within a median of two weeks before infusion, two patients had overt disease, five were MRD-positive and the rest had no evaluable disease (NED) (Supplementary Fig. 2). Ten patients received EBV-specific T_{TCR-C4} and five received CMV-specific T cells (Table 1). Patients received one to four infusions depending on their place in the T_{TCR-C4} dose escalation (Supplementary Fig. 3).

As in Arm 1¹³, T_{TCR-C4} infusions were safe and well tolerated (Supplementary Table 2). The incidence of acute and chronic GVHD (aGVHD, cGVHD) was lower compared to DLIs or second HCTs as salvage strategies^{14,29}, with only one patient (-7%) developing grade 3 aGVHD and one (-7%) developing moderate cGVHD post-T_{TCR-C4} infusion. Similarly to our prophylactic arm¹³, a biopsy obtained at the time of cGVHD showed lower T_{TCR-C4} frequencies in tissue (~0.08% of total CD3⁺ T cells) (Supplementary Fig. 4) compared to PB (60/mcL, ~8% of total CD8⁺ T cells), suggesting no correlation between PB T_{TCR-C4} concentration and tissue GVHD.

Among the patients enrolled, four showed no overt relapse and/or MRD following T_{TCR-C4} infusion(s) (Supplementary Fig. 5) supporting T_{TCR-C4}'s potential biologic activity. However, when all 15 patients were analyzed together, the median OS was 242 days, the 2-year OS was 33%, and the 3-year OS was 20% (Supplementary Fig. 6), indicating that these individual outcomes did not translate into a significant survival advantage over historical salvage treatments^{1,2,14,15}. For example, DLI post-HCT relapse showed a 2-year OS of 21% (± 3%) from relapse and 56% (± 10%) from DLI in cases of remission or with a favorable karyotype, dropping to 15% (± 3%) in aplasia or active disease²⁹.

Table 1 | Clinical characteristics of AML patients receiving T_{TCR-C4} infusions

Pt	AML WT1 expression	Disease status 28 days post-HCT	Number of HCT before T _{TCR-C4} infusion	Salvage therapy before T _{TCR-C4} infusion	Lymphodepletion	Disease status at 1 st T _{TCR-C4} infusion	Days between salvage and T _{TCR-C4} infusion	Virus specificity	T _{TCR-C4} infusions received
1	NA	NED	1	Yes	No	NED	87	EBV	3
2	Yes	NED	2	Yes	No	MRD	60	CMV	4
4	Yes	NED	2	Yes	No	NED	89	EBV	2
5	Yes	MRD	1	No	No	Overt		EBV	1
6	NA	NED	2	Yes	No	NED	59	CMV	4
7	No	MRD	1	Yes	No	MRD	33	EBV	1
8	Yes	MRD	1	No	No	MRD		EBV	2
9	Yes	MRD	1	Yes	No	MRD	52	CMV	4
14	Yes	NED	2	Yes	No	MRD	61	EBV	2
15	No	NED	2	Yes	No	NED	110	CMV	2
19	Yes	NED	1	Yes	No	Overt	243	EBV	1
23	Yes	NED	1	Yes	No	NED	246	EBV	1
26	Yes	NED	1	Yes	Yes	NED	53	EBV	2
27	Yes	NED	1	Yes	Yes	NED	178	EBV	1
28	Yes	NED	2	Yes	Yes	NED	31	CMV	2

AML Acute Myeloid Leukemia, HCT Hematopoietic Cell Transplantation, NED No Evidence of Disease, MRD Measurable Residual Disease, EBV Epstein-Barr Virus, CMV Cytomegalovirus. This table summarizes the clinical data of patients with AML relapsed/refractory after HCT, who received T_{TCR-C4} infusions.

Virus-specific substrate T cells and AML presence at the time of infusion are major determinants of T_{TCR-C4} persistence

In our cohort, baseline PB WT1-specific tetramer⁺ T cells were low (Fig. 1A—red arrows, day 0) indicating limited endogenous WT1-specific T cells. By day 28 post-infusion, four patients showed T_{TCR-C4} levels exceeding 3% of the CD8⁺ T cells (persistence threshold), with three maintaining these levels beyond day 100. Patients with T_{TCR-C4} frequencies below 3% were eligible for additional infusions (two infusions in 6/15 patients, >2 infusions in 4/15 patients) (Table 1). However, more than two infusions did not significantly increase persistence (Fig. 1B).

We next explored the contribution of substrate cell virus-specificity to post-infusion persistence. Within 28 days, EBV-specific T_{TCR-C4} were more abundant than CMV-specific T_{TCR-C4}, which remained below the persistence threshold (Fig. 1C). These differences endured when EBV-specific T_{TCR-C4} recipients from Arm 1 were included (Supplementary Fig. 7)¹³. As central-memory CD8⁺ T cells (Tcm) have shown improved persistence compared to more differentiated phenotypes post-transfer³⁰, we sought to explore whether differences in endogenous virus-specific cells could recapitulate these findings. We analyzed the phenotypes of EBV- and CMV-specific T cells using mass cytometry data³¹ from 143 healthy individuals and cancer patients. Multidimensional scaling (MDS) showed segregation of CMV- and EBV-specific CD8⁺ T cells along the first dimension (MDS dim.1) suggesting distinct T-cell differentiation states between these groups (Supplementary Fig. 8A). Next, Flow Self-Organizing Maps (FlowSOM)³² metaclustering identified four CD8⁺ T-cell subsets: naïve (CD95⁺, CD45RA⁺, CCR7⁺, CD27⁺, CD28⁺), effector memory (Tem) (CD95⁺, CD45RA⁻, CD45RO⁺, CD27⁺, CD28⁺, CD127⁺), Tcm (CD95⁺, CD45RA⁻, CD45RO⁺, CCR7⁺, CD27⁺, CD28⁺, CD127⁺), CD45RA⁺ effector memory (Temra) (CD95⁺, CD45RA⁺, CD45RO⁻, CD57⁺, KLRG1⁺) (Supplementary Fig. 8B)^{33,34}. Differential abundance analysis revealed a significant (false discovery rate/FDR < 0.05) increase of Temra cells in CMV-specific T cells and of naïve, Tcm and Tem in EBV-specific T cells (Fig. 1D, and Supplementary Fig. 8C). These results suggest that the Temra state of CMV-specific substrate cells compromises post-infusion persistence, whereas EBV-specific cells, derived from less differentiated precursors, facilitate persistence.

Persistence varied among EBV-specific T_{TCR-C4} recipients (Fig. 1C), with only three of ten exhibiting long-term persistence (>100 days post-infusion) (Fig. 1A, and Supplementary Fig. 9). We reasoned that persistence was influenced by AML high-risk factors, including post-transplant remission duration and disease burden at the time of T_{TCR-C4} infusion³. Patient 1 was excluded from this analysis due to unavailable WT1-expression data. Six of the remaining patients did not show long-term persistence: four (5,7,14, and 19) had detectable disease (MRD or overt) within two weeks of T_{TCR-C4} infusion, and two (23, 26) who were disease-free at infusion, had relapsed within 3 months post-HCT, suggesting difficult-to-control disease. Statistical testing revealed a trend (Fisher's exact test, $p = 0.08$) linking reduced persistence with these high-risk clinical factors (detectable disease pre-infusion or early relapse post-HCT). Patient 8, initially MRD-positive before the first infusion, became MRD-negative through salvage therapy before the second infusion, achieving the longest observed T_{TCR-C4} persistence. Reclassifying this patient with the MRD-/non-early relapse group, renders the association between disease risk factors and persistence statistically significant ($p < 0.05$) (Supplementary Fig. 10). Notably, cell blood counts and blasts percentage did not significantly correlate with persistence (Supplementary Table 3). These findings suggest that aggressive disease post-HCT, independently of virus-specificity, was associated with reduced T_{TCR-C4} persistence in vivo.

Long-term persistent T_{TCR-C4} acquire NKL/terminal differentiation markers associated with progressive loss of function in vivo

To investigate the fate of T_{TCR-C4} post-transfer in patients with persistent T_{TCR-C4}, and compare these with endogenous (TCR_{C4}⁻) T cells,

we used a validated^{24,25} 24-color spectral flow-cytometry panel (Supplementary Table 4). PB was analyzed at -1 (T1), -7 (T2), 28 (T3) days, and -4 months (T4) post-transfer (Supplementary Table 5). FlowSOM clustering revealed five CD8⁺ T-cell states categorized into three higher-level clusters (Fig. 2A, top dendrogram): naïve/cm-like cells (Fig. 2A, dark green) (CD45RA⁺, CCR7⁺, CD27⁺, CD28⁺); Tem subgroup, including endogenous CD8⁺ Tem (CD28⁺, CD27⁺, Ki67⁺, CD38⁺, TIGIT⁺, PD1⁺, Tbet⁺) (Fig. 2A, violet), and phenotypically similar T_{TCR-C4}_Tem (tetramer⁺) (Fig. 2A, blue); Temra subgroup of endogenous CD8⁺ T cells (CD45RA⁺, CD57⁺, KLRG1⁺, GZMB⁺) (Fig. 2A, light green) and closely clustered T_{TCR-C4}_Temra (Fig. 2A, red). Two-dimensional Uniform Manifold Approximation and Projection (UMAP) revealed a progressive increase in T_{TCR-C4}_Temra and decline in T_{TCR-C4}_Tem from T1 to T4 (Fig. 2B). T_{TCR-C4}_Temra expressed minimal Ki67 compared to T_{TCR-C4}_Tem (Fig. 2A), enabling manual gating of these two subsets (Fig. 2C, and Supplementary Fig. 11). Over time, T_{TCR-C4}_Temra significantly increased, while T_{TCR-C4}_Tem decreased ($p < 0.05$) (Fig. 2D), suggesting differentiation from proliferative T_{TCR-C4}_Tem to non-proliferative T_{TCR-C4}_Temra. T_{TCR-C4}_Temra predominantly expressed cytotoxic/KLR markers (KLRG1, CD57, GNLY), previously linked to T-cell dysfunction in AML^{24,25}, rather than classical T-cell exhaustion markers (Tim3, PD1, and TIGIT) (Fig. 2E)^{20,35}. Stratification by timepoint revealed progressive increase of the cytotoxic subset versus the exhausted subset (Fig. 2F). This phenotypic shift coincided with a significant decline over time in T_{TCR-C4} CD8⁺ T cells producing IFN γ (Fig. 2G, and Supplementary Fig. 12, 13, Supplementary Table 6). Production of IFN γ by Tet⁻ cells (negative control) was near undetectable (Supplementary Figs. 12, 13).

Previous work³⁶ showed that NK skewing of CAR-T cell products correlates with increased innate-like serum cytokines. Although none of the 49 cytokines we tested showed a significant increase over time, the pro-inflammatory cytokine IL-18 exhibited an increasing trend (Supplementary Fig. 14, and Supplementary Table 7), consistent with previous findings³⁶. Notably, the reported changes in IL-15 concentration were below the threshold limit of detection of our assay (3.84 pg/ml). It is possible that changes in IL-15 concentration still occur in this context, but they were not detectable by our assay.

Overall our findings show that long-term persisting EBV-specific T_{TCR-C4} skew towards a distinct NKL phenotype linked to functional decline.

Single-cell profiling of CD8⁺ T cells reveals distinct immune states of endogenous and T_{TCR-C4} cells

To explore the relationship between CD8⁺ endogenous T-cell and T_{TCR-C4} states, we performed single-cell RNA sequencing (scRNAseq) on available PB and bone marrow (BM) samples from patients with T_{TCR-C4} $\geq 3\%$ of CD8⁺ T cells at day 28 or later after first infusion. This analysis included two prophylactic¹³ and five treatment-arm patients (Supplementary Table 8).

Unsupervised clustering of PB CD8⁺ T cells ($n = 24,472$) identified 13 clusters, with the TCR_{C4} transgene expressed across several clusters, but primarily in cluster 2 (Fig. 3A). Using the marker-based purification algorithm scGate³⁷, we identified TCR_{C4}⁺ cells (Fig. 3B) labeled as T_{TCR-C4}, while endogenous (TCR_{C4}⁻) T cells included clusters 5 and 6, labeled as naïve/cm-like, expressing *CCR7*, *SELL*, *TCF7*, *LEF1*, *IL7R*; clusters 2, 4 and 11, labeled as Tem, expressing genes associated with activation (*CD69*, *TIGIT*, *GZMK*); cluster 12, labeled as interferon signaling genes (ISG), expressing *ISG15*, *ISG20*, *IRF7*, *IFI6*; clusters 9 and 10, labeled as T memory/proliferative (Tmem/prolif), expressing proliferation (*MKI67*, *MCM5*, *MCM7*) and memory (*CD27*) genes; clusters 0,1,3,7, and 8, labeled as NKL/Temra, expressing genes associated with cytotoxicity/NKL (*KLRF1*, *KIR3DL1*, *NG7*, *FCGR3A*, *GZMB*, *KLRD1*, *PRF1*) (Fig. 3A–E, and Supplementary Fig. 15A)^{33,34,38–40}.

To assess transcriptional similarities among cell states, we performed principal component analysis, positioning naïve/cm-like and

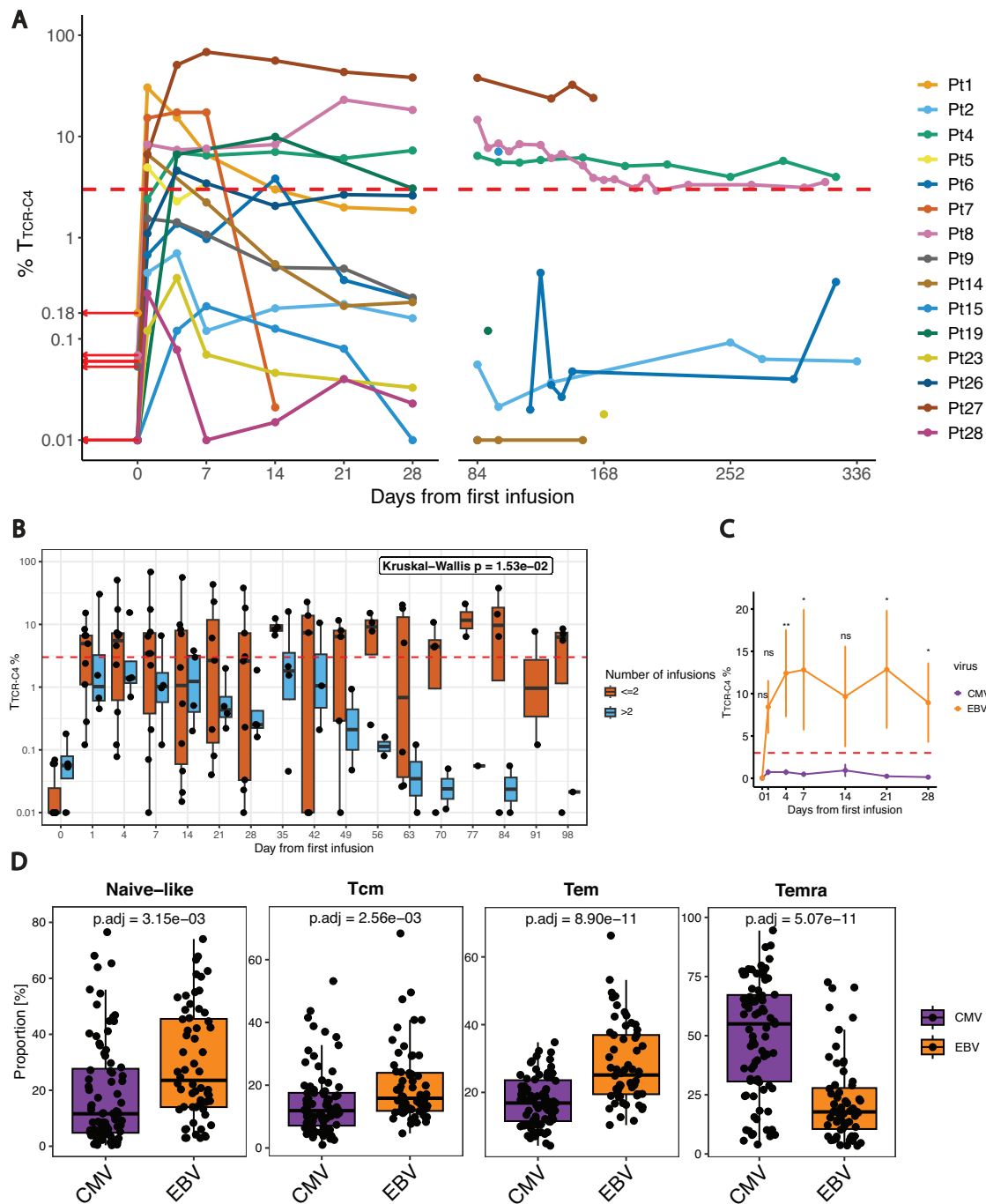
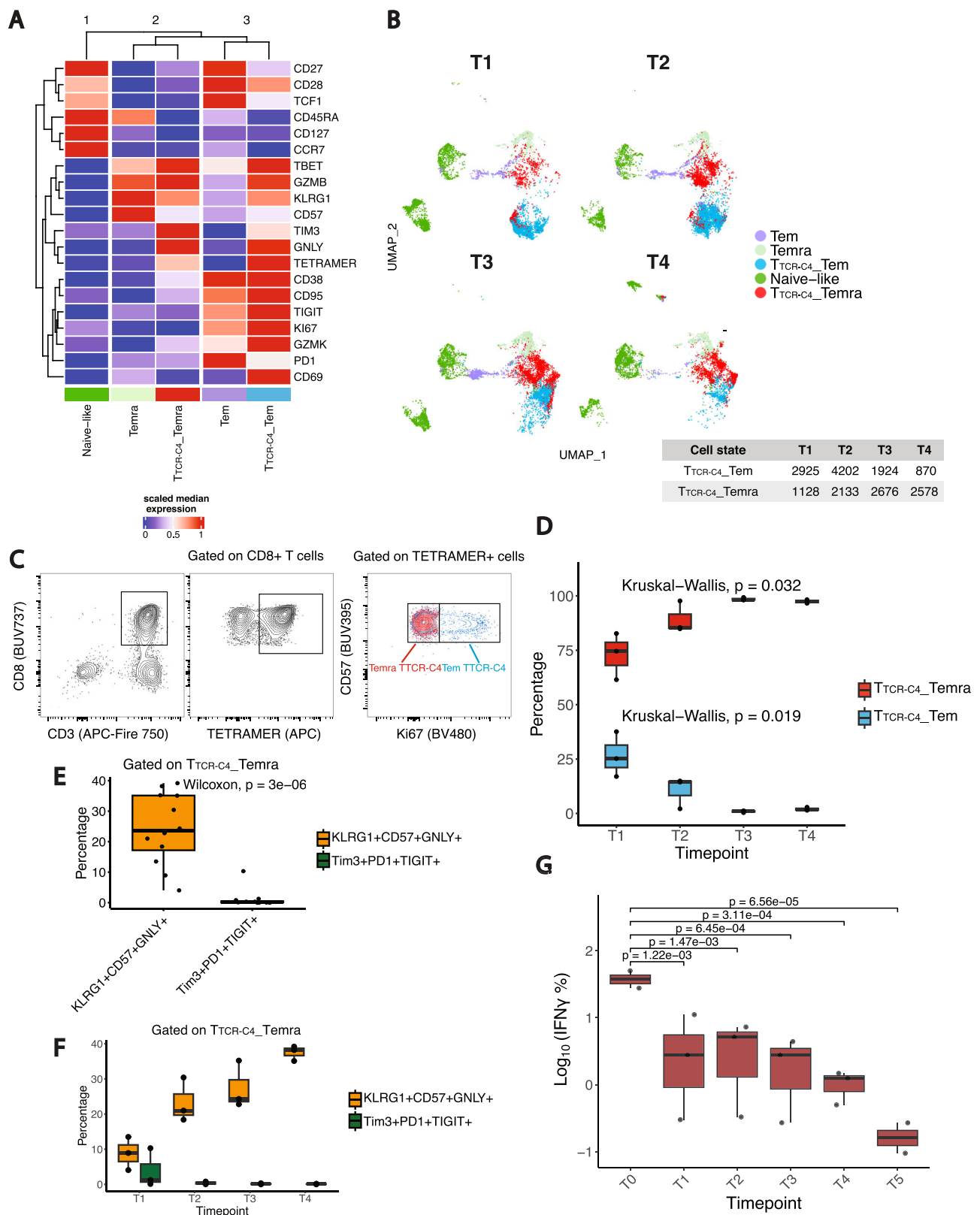


Fig. 1 | Virus-dependent terminal differentiation skewing of T_{TCR-C4} . **A** Line plot showing the percentage (log scale, y-axis) of T_{TCR-C4} in PBMCs after the first T_{TCR-C4} infusion for all patients ($n = 15$). Data points represent individual samples at different timepoints post-infusion. Each patient is represented by a distinct color. Red arrows indicate WT1-specific $CD8^+$ T cells percentages at day 0. The dashed red line indicates the 3% threshold used to define persisting T_{TCR-C4} cells. **B** Boxplots comparing T_{TCR-C4} percentages (log scale, y-axis) post-first infusion (x-axis) in all patients ($n = 15$), colored by the number of infusions (light blue: ≤ 2 ; dark orange: > 2). The dashed red line indicates the 3% threshold used to define persisting T_{TCR-C4} cells. Statistical significance was determined using Kruskal-Wallis test, with $p < 0.05$ considered significant. Boxplots show the interquartile range (IQR); lines denote medians. The bounds of the box represent the 25th and 75th percentiles; whiskers span $1.5 \times$ IQR. **C** Line plot of T_{TCR-C4} percentages (y-axis) derived from EBV-specific (dark orange) or CMV-specific (dark violet) substrate cells over a 28-day period (x-axis).

axis) post-first infusion ($n = 15$). Error bars indicate mean \pm standard error of the mean. Statistical significance was determined using a two-sided Wilcoxon Rank Sum test. (* $p < 0.05$, ** $p < 0.01$). Significant differences were observed at days 4 ($p = 0.00699$), 7 ($p = 0.012$), 21 ($p = 0.0303$), and 28 ($p = 0.0295$). **D** Boxplots showing differential abundance analysis of CMV-specific (dark violet) and EBV-specific (dark orange) $CD8^+$ T-cell subsets derived from the analysis of mass cytometry data ($n = 143$). $CD8^+$ T-cell subsets are defined based on marker co-expression shown in Supplementary Fig. 8B. Differential abundance between conditions (CMV vs. EBV) was computed using the edgeR method within the diffcyt framework. P -values were adjusted for multiple testing using the Benjamini-Hochberg procedure. Adjusted p -values (threshold for significance of $p < 0.05$) are displayed above each comparison. Boxplots show the IQR; lines denote medians. The bounds of the box represent the 25th and 75th percentiles; whiskers span $1.5 \times$ IQR.



NKL/Temra as differentiation spectrum extremes, with T_{TCR-C4} as the intermediate state between these two extremes (Fig. 3D). Next, to ensure unbiased labeling of $CD8^+$ T cells, we constructed a scRNAseq reference atlas comprising 109,051 $CD8^+$ T cells, using a published scRNAseq dataset of tumor-infiltrating lymphocytes⁴¹. We aligned and projected our scRNAseq dataset onto the reference atlas (Supplementary Fig. 15B), confirming the correspondence between the

transcriptional states in our dataset and the reference. Differential gene expression (DGE) analysis using manually curated markers further supported this annotation (Supplementary Table 9, Fig. 3E)^{33,34,38,39}.

Consistent with previous work³⁴, we observed a progressive reduction of stem-like markers (*IL7R*, *TCF7*) from naive/cm-like cells through Tem and NKL/Temra cells, while activation markers (*CD69*,

Fig. 2 | CD8⁺ T cell subset phenotypes and functional states over time.

A Heatmap of fluorescence intensity for 20 markers across Naïve-like, Tem, T_{TCR-C4}-Tem (tetramer⁺), Temra, T_{TCR-C4}-Temra (tetramer⁺) PB CD8⁺ T cells. Median expression values are highlighted (red = high, blue = low). Data were scaled post-aggregation to highlight population-level differences between tetramer⁺ and tetramer⁻ samples. K-means algorithm categorized clusters by similarity into three groups (1-3, top of heatmap). Data were derived from spectral flow-cytometry. **B** UMAP plots of the CD8⁺ T-cell subsets, colored by subset and split by timepoint. The table shows the absolute numbers of T_{TCR-C4}-Tem and T_{TCR-C4}-Temra cells at timepoints T1-T4. **C** Contour plots illustrating the gating strategy for T_{TCR-C4}-Tem (blue) and T_{TCR-C4}-Temra (red); CD3⁺CD8⁺ were first gated, followed by selection of tetramer⁺ cells, and finally separation based on Ki67 expression: Ki67⁺ (T_{TCR-C4}-Tem, blue) and Ki67⁻ (T_{TCR-C4}-Temra, red) cells. This strategy was based on marker expression in Fig. 2A. **D** Boxplots of T_{TCR-C4}-Tem and T_{TCR-C4}-Temra percentages over time (T1-T4, *n* = 3). Statistical significance was assessed using Kruskal-Wallis

test. Boxplots show the IQR; lines denote medians. The bounds of the box represent the 25th and 75th percentiles; whiskers span 1.5x IQR. **E** Boxplots showing cytotoxic (KLRG1⁺, CD57⁺, GNLY⁺; dark red) vs. exhausted (TIM3⁺, PDI⁺, TIGIT⁺; blue) T cells among T_{TCR-C4}-Temra (*n* = 3). Statistical significance was assessed using a two-sided Wilcoxon rank-sum test. Boxplots show the IQR; lines denote medians. The bounds of the box represent the 25th and 75th percentiles; whiskers span 1.5x IQR. **F** Boxplots displaying cytotoxic (dark red) vs. exhausted (blue) T cells among T_{TCR-C4}-Temra over time (T1-T4, *n* = 3). Boxplots show the IQR; lines denote medians. The bounds of the box represent the 25th and 75th percentiles; whiskers span 1.5x IQR. **G** Boxplots showing log10-transformed percentages of T_{TCR-C4} IFNγ⁺ cells within the CD8⁺ population following WT1-peptide stimulation across timepoints post-first infusion (*n* = 3, Supplementary Table 6). A linear mixed-effects model assessed the effect of Timepoint (T0 as intercept) on IFNγ production, with a two-sided hypothesis test. Boxplots show the IQR; lines denote medians. The bounds of the box represent the 25th and 75th percentiles; whiskers span 1.5x IQR.

GZMK) peaked in Tem. NKL markers, including KLR-exhaustion markers (*SIPR5*, *ZEB2*)^{42,43}, were highest in NKL/Temra. (Supplementary Fig. 15C). These results were confirmed through pairwise DGE between T_{TCR-C4} and endogenous NKL/Temra. T_{TCR-C4} expressed genes associated with activation (*GZMK*, *LTB*, *GNLY*) and memory (*IL7R*, *CD27*), while NKL/Temra cells expressed cytotoxicity (*GZMH*, *PRFI*) and NKL/Temra genes (*KLF3*, *FCGR3A*, *ZEB2*, *SIPR5*) (Fig. 3F)^{26,36,42-44}. These findings align with previous CAR-T cell studies³⁶, and suggest that T_{TCR-C4} expressing activation and NKL markers represent an intermediate state between Tem and NKL/Temra.

Clonal differentiation and trajectory analysis reveal T_{TCR-C4} as an intermediate state in CD8⁺ T cell differentiation

To analyze T-cell differentiation dynamics we used Monocle trajectory⁴⁵ and RNA velocity⁴⁶ inference. This analysis confirmed T_{TCR-C4} as an intermediate state between Tem and the terminal NKL/Temra state (Fig. 4A-C), and removing the TCR_{C4} transgene did not alter this differentiation trajectory (Supplementary Fig. 16A, B). Next, to explore clonal differentiation dynamics, we analyzed the TCR sequencing from our dataset (Supplementary Table 8). Similarly to previous findings^{25,36}, the most clonally expanded subsets were T_{TCR-C4} and endogenous NKL/Temra cells (Fig. 4D). We then employed TCR amino acid sequences to trace differentiation pathways, hypothesizing that T cells differentiate progressively as they clonally expand. Using shared TCR sequences across clusters, we inferred trajectories by tracking transitions from less expanded to more expanded populations (Fig. 4E). Clonally expanded T_{TCR-C4} upregulated NKL/cytotoxicity genes, suggesting skewing towards the NKL phenotype concomitant with clonal expansion (Fig. 4F). This analysis highlighted a distinct clonal differentiation pattern of endogenous and T_{TCR-C4} progressing towards NKL/Temra.

Single-gene expression over pseudotime revealed early peaks of naïve/stem-like markers (*CCR7*, *IL7R*, *TCF7*, *SELL*, *LEF1*) (Supplementary Fig. 17, first row), naïve/memory (*CD27*, *CD28*) and activation markers (*GZMK*, *CD69*), with the latter remaining high throughout mid-pseudotime before declining (Supplementary Fig. 17, second row). TCR_{C4} expression peaked at mid-pseudotime, but remained expressed until the end of pseudotime. NKL/Temra-associated genes (*PRFI*, *KLRG1*, *NKG7*, *ZEB2*, *SIPR5*) peaked at the end of pseudotime (Supplementary Fig. 17, third row). Smoothed gene expression analysis of endogenous (TCR_{C4}⁻) and TCR_{C4}⁺ cells revealed an increase in NKL/cytotoxicity markers along pseudotime. At the start of the pseudotime trajectory, endogenous TCR_{C4}⁻ cells predominantly expressed naïve/cm-like genes (*CCR7*, *SELL*, *LEF1*), consistent with the presence of naïve endogenous CD8⁺ T cells. In contrast, ex vivo expanded TCR_{C4}⁺ cells lacked naïve markers. As the trajectory progressed, the expression of naïve/cm-like genes became comparable between the two groups (Fig. 4G).

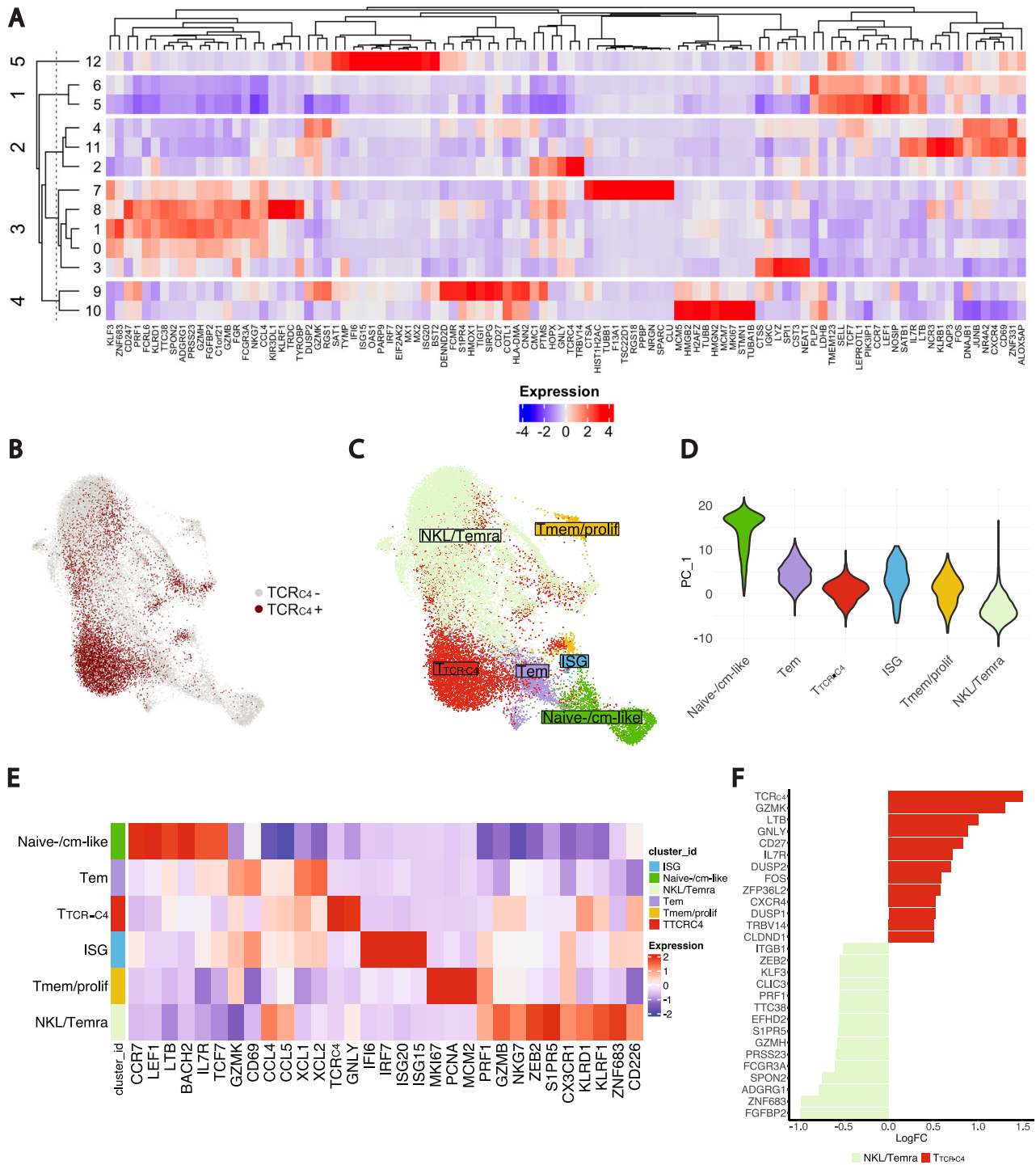
Overall, our findings suggest that T_{TCR-C4} largely existed in an intermediate state between the Tem phenotype and the NKL/Temra stage.

AML drives T_{TCR-C4} towards NKL/terminal differentiation instead of the dominant exhaustion pattern associated with T cells in solid tumors

To investigate AML's impact on the differentiation of endogenous CD8⁺ T cells and T_{TCR-C4}, patients samples were grouped as AML- (no AML detected, including two prophylactic arm cases)¹³, or AML+ (blasts evident in BM and/or PB) (Supplementary Table 10, and Supplementary Fig. 18A, B). The increase of ISG and NKL/Temra in AML+ and T_{TCR-C4} in AML- (Fig. 5A) was significant (Fig. 5B), with a wide confidence interval for ISG, making the magnitude of this difference unclear. T_{TCR-C4} overexpressed NKL/Temra genes in AML+ compared to AML- (Fig. 5C), suggesting that AML blasts may induce a transcriptional shift towards NKL/Temra in T_{TCR-C4} and endogenous T cells.

Next, we evaluated previously described T-cell dysfunction signatures^{25,47,48} and found that progenitor exhausted (Tpex) signatures were enriched in naïve/cm-like and Tem, while Terminally exhausted (Ttex) signatures were enriched in Tmem/prolif (Supplementary Fig. 19A). However, intersecting these signatures with the top 50 differentially expressed genes per subset, revealed limited overlap (*IL7R*, *LEF1*, *SELL*, *CCR7*, *TCF7*, *FOXPI*, *FOS*) for Tpex and naïve/cm-like, three genes (*CXCR4*, *NR4A2*, *JUN*) for Tpex and Tem, and only *TYMS* for Ttex and Tmem/prolif. The absence of canonical markers of exhaustion suggests that these subsets do not predominantly express this program. In contrast, NKL/Temra showed significant overlap with previously published signatures of NKL skewing (Supplementary Fig. 19B, and Supplementary Table 11)²⁵. Additionally, T_{TCR-C4} in the setting of AML+ samples showed hyperexpression of NKL instead of exhaustion genes (Supplementary Fig. 19C). These findings align with a previous report in large B-cell lymphoma showing that terminally differentiated CD57⁺ CAR-T cells with senescence features can transition to an NK-like rather than exhaustion program⁴⁰. We also projected scores from published NKL signatures^{25,42,43} onto our UMAP, revealing overlaps that link the NKL/Temra CD8⁺ T cells we identified with an end-term differentiation subset (Supplementary Fig. 19D).

To clarify whether AML-induced dysfunction aligns with T-cell exhaustion or NKL skewing, we used a previously described model²⁶. We exposed in vitro CD8⁺ transgenic WT1-specific T cells targeting the HLA A*0201-restricted WT1₃₇₋₄₅ epitope (T_{TCR37-45}) to high-WT1-expressing HLA-A*0201-transduced K562 acutely transformed chronic myelogenous leukemia (Supplementary Fig. 20A). As K562 primarily express standard proteasomes and are not readily lysed by T_{TCR-C4} targeting the immunoproteasome-specific WT1₁₂₆₋₁₃₄ peptide, we used T_{TCR37-45} due to its proteasome-agnostic WT1-derived peptide recognition⁴⁹. Exposing T_{TCR37-45} to fresh K562 every 3-4 days at stable



effector-to-target (E:T) ratios (1:1, 1:4) caused initial tumor lysis (Fig. 5D), but control was lost by day 13, marked by a declining $T_{TCR37-45}$ -to-tumor ratio (Fig. 5E). Irrelevant TCR-expressing T cells exerted no control (Supplementary Fig. 20B). Bulk-RNA sequencing on sorted T cells (Supplementary Fig. 21) found increased (FDR < 0.05) naïve/stem-like genes (*IL7R*, *TCF7*, *LTB*, *LEF1*, *SELL*) at day 0, followed at day 13 by increased effector (*CCL5*, *GZMK*), activation/exhaustion (*CD69*, *LAG3*, *CTLA4*, *PDCDI*), and NKLTemra markers (*KLRB1*, *ENTPD1*, *KLRC1*, *KLRC2*, *NCAMI*) (Fig. 5F-H). By day 23, the activation/exhaustion markers decreased, while NKLTemra persisted or increased (Fig. 5F-H). To integrate these findings with the scRNAseq dataset, we performed a gene-set enrichment analysis with the top 50 differentially expressed

genes from each CD8⁺ subset identified in scRNAseq, including naïve/cm-like, Tem, NKLTemra, T_{TCR^{C4} , Tmem/prolif and ISG from the scRNAseq dataset. We also included a manually curated exhaustion signature (Supplementary Table 12). Exhaustion and Tem signatures exhibited enrichment in later timepoints, yet there was no further increase at day 23 versus day 13 (Fig. 5H). In contrast, the NKLTemra increased between days 13 and 23 corresponding to $T_{TCR37-45}$ loss of tumor control (Fig. 5E).

We performed GSEA on the scRNA-seq data to assess whether T_{TCR^{C4} cells lose antigen reactivity and tumor control as they differentiate into NKLTemra cells. Our analysis showed no significant differences between NKLTemra and non-NKLTemra T_{TCR^{C4} states (Supplementary

Fig. 3 | Single cell transcriptomic analysis of endogenous and $T_{TCR-C4} CD8^+$ T-cell states and their differentiation dynamics. **A** Heatmap showing the top 10 differentially expressed genes per cluster. The “top 10” refers to the 10 genes with the most significant differential expression across the identified clusters. The dendrogram on the left displays the similarity between the 13 clusters, which were determined through unsupervised clustering based on gene co-expression patterns. The top dendrogram shows the relationships between the genes based on their expression patterns. K-means algorithm grouped the 13 clusters into 5 main categories, labeled 1 to 5 on the left side of the heatmap. Blue indicates low expression; red, high. **B** UMAP plot of the $CD8^+$ T cells (endogenous and T_{TCR-C4}^+) on a two-dimensional space. T_{TCR-C4}^+ cells were identified using scGate, an R package which scores cells based on TCR_{C4} expression and defines thresholds to classify cells as positive or negative for the population of interest. TCR_{C4}^+ cells are colored in dark red, while TCR_{C4}^- cells (endogenous) are represented in light gray. **C** UMAP plot displaying the two-dimensional distribution of annotated $CD8^+$ T-cell transcriptional states, colored by subset. **D** Violin plot illustrating the distribution

of $CD8^+$ T-cell subsets identified through gene expression (Fig. 3A) and TCR_{C4} score (Fig. 3B) along the principal component 1 (PC₁) axis. Each violin represents a different $CD8^+$ T-cell state. The proximity of each subset along PC₁ (y-axis) indicates transcriptional similarity, with subsets closer together showing more similar gene expression profiles. **E** Heatmap showing the differential expression of manually curated genes across the five annotated $CD8^+$ T-cell subsets. Blue and red indicate the relative expression levels of each marker within each subset, with blue representing lower expression and red indicating higher expression. **F** Bar plot showing differential gene expression analysis comparing T_{TCR-C4} and NKL/Temra (T_{TCR-C4}^-) $CD8^+$ T cells. Differential expression was performed using a two-sided Wilcoxon rank-sum test implemented in the Seurat package. *P*-values were adjusted for multiple testing using the Bonferroni correction. Genes with an adjusted *p*-value (*padj*) < 0.01 and log₂ fold change (log₂FC) > 0.5 or < -0.5 were included. Bars represent log₂ fold change values, with red indicating genes upregulated in T_{TCR-C4} and green representing genes upregulated in NKL/Temra.

Fig. 22A, B), and TCR signaling genes were not downregulated in NKL T_{TCR-C4} cells compared to non-NKL T_{TCR-C4} cells (Supplementary Fig. 22C, D).

To confirm that AML-exposed T cells skewed towards a NKL/Temra rather than exhausted (Tex) phenotype, we projected onto a scRNAseq reference atlas⁴¹ a BM AML $CD8^+$ T-cell dataset, compiled from published sources^{23,25,50–52}, alongside datasets representing pancreatic⁵³, melanoma⁵⁴, and lung⁵⁵ solid tumors (Supplementary Fig. 23A, B). Unlike solid tumors, which included a Tex cluster, AML datasets aligned with our spectral flow-cytometry and scRNAseq findings confirming the absence of Tex and the presence of NKL/Temra cells (Supplementary Fig. 23C). Although these studies did not specifically analyze tumor-antigen reactive T cells, the findings collectively suggest that the NKL (versus exhaustion) signature is intricately associated with AML-induced T-cell dysfunction.

Prolonged azacitidine exposure enhances self-renewal and Tcm features of T_{TCR-C4} , supporting T_{TCR-C4} -mediated AML control

Given the link between NKL differentiation and AML-induced T-cell dysfunction, we explored the state of T_{TCR-C4} in patient 8, the only patient of 4 (Supplementary Fig. 5) who exhibited prolonged T_{TCR-C4} and MRD persistence indicative of disease control despite incomplete leukemia clearance, enabling T_{TCR-C4} /AML interplay analysis. This female patient underwent a non-myelo-ablative (Flu/3Gy-TBI) HCT from a male donor, with MRD (0.26% blasts by flow cytometry) detected 28 days post-HCT (Fig. 6A) and received T_{TCR-C4} (10^{10} cells/ m^2) 77 days post-HCT. AML blasts expressed detectable but limited WT1 protein pre-HCT (Supplementary Fig. 24). scRNAseq at day 49 post-infusion revealed circulating $CD34^+$ female-origin blasts (XIST⁺) expressing WT1 (Fig. 7A, B). Persistent MRD and limited T-cell persistence at day 63 post-infusion (T cells declined to only 0.1 multimer⁺ $CD8^+$ T cells/ μ l on day 60), (Figs. 6B, 6C-red arrow, 6D) prompted azacitidine treatment (five days every 28 days). Post-azacitidine, T_{TCR-C4} counts increased (-50 multimer⁺ $CD8^+$ T cells/ μ l; >3% $CD8$ multimer⁺ T cells) without additional T_{TCR-C4} (Fig. 6D), leading to azacitidine discontinuation after seven cycles when no AML was detected. However, AML recurrence at day 414 post-infusion triggered chemotherapy (mitoxantrone, etoposide and cytarabine), additional azacitidine cycles followed by a second T_{TCR-C4} (10^{10} cells/ m^2) infusion (Fig. 6A). Azacitidine was held post-infusion but restarted upon MRD detection 162 days post-second T_{TCR-C4} infusion, continuing for over 20 monthly cycles, maintaining marrow MRD below 1% for 21 months (641 days, from day 868 to day 1509) before progression was detected on day 1546 (Fig. 6A, B). During this 21-month period, blasts were detectable via scRNAseq in BM but not in PB (Fig. 7B, and Supplementary Fig. 25A, B). Throughout the azacitidine cycles, platelet counts decreased (-100×10^3 platelets/ μ l) mid-cycle before rising (-300×10^3 platelets/ μ l) immediately before the next cycle, consistent

with transient azacitidine-mediated myelosuppression. Neutrophil counts, however, paradoxically increased mid-cycle (-4.5×10^3 neutrophils/ μ l) and decreased (-1.6×10^3 neutrophils/ μ l) just before the next cycle, suggesting that treatment-related AML contraction facilitated enhanced mid-cycle neutrophil production despite azacitidine's myelosuppressive effect (Supplementary Fig. 25C). This 21-month response exceeds the typical 4-month median for post-HCT azacitidine treatment⁵⁶, suggesting that persisting T_{TCR-C4} plus azacitidine contributed to long-term disease control.

T_{TCR-C4} transcriptomics were analyzed to identify associations with disease control. We scored genes associated with self-renewal and NK-like profiles and found that at earlier timepoints (d49, d256, and d405 post-first infusion), T_{TCR-C4} were predominantly skewed towards an NKL/Temra transcriptional state. However, at later timepoints (d1322, d1343) although T_{TCR-C4} remained along the same differentiation trajectory (from less differentiated states to NKL/Temra T_{TCR-C4}), they exhibited fewer NKL features, and showed an enrichment of self-renewal markers (Fig. 7C–F). scTCRseq analysis of PB at days 265, 405, 1322, 1343 post-first T_{TCR-C4} infusion revealed progressive clonal expansion of T_{TCR-C4} (Fig. 7G). T_{TCR-C4} clonal expansion peaked during the 21 months of continued azacitidine treatment, suggesting that during this phase, T_{TCR-C4} were capable of both self-renewal, which in turn facilitated their long-term persistence, and antigen recognition, which triggered further expansion and disease control. Similarly, BM scRNAseq revealed clonal expansion of T_{TCR-C4} between d1322 and d1344 post-first infusion (Fig. 7H) despite no additional T_{TCR-C4} . To reproduce this in vitro, we induced T_{TCR-C4} differentiation (see “Methods”) in the presence or absence of azacitidine. After 14 days of stimulation, we observed that the presence of azacitidine significantly (*p* < 0.05) reduced the skewing towards $CD57^+KLRG1^+$ T_{TCR-C4} (Fig. 7I, and Supplementary Fig. 26, Supplementary Table 13). $CD8^+CD57^+KLRG1^+$ cells have previously been shown to exhibit an NKL transcriptional profile²⁵ and reduced leukemia cell killing capabilities²⁴. With the caveat that the evidence is based on one patient, these findings suggest that azacitidine-exposed T_{TCR-C4} , retained self-renewing (versus NKL) features, which may have supported their long-term persistence and enhanced AML-targeting efficacy that may have contributed to long-term disease control (Fig. 7J).

Discussion

We previously demonstrated that EBV-specific T_{TCR-C4} infusion appears to prevent AML recurrence leading to a survival advantage in patients at high risk of post-HCT relapse¹³. In the current study, among 15 AML patients who received T_{TCR-C4} post-HCT relapse, we observed indirect evidence supporting anti-leukemic activity but found no survival advantage in patients receiving either EBV- or CMV-specific $CD8^+$ T cells engineered to express TCR_{C4} . We analyzed the AML/ T_{TCR-C4} interplay to investigate how AML affects antigen-specific T cells and

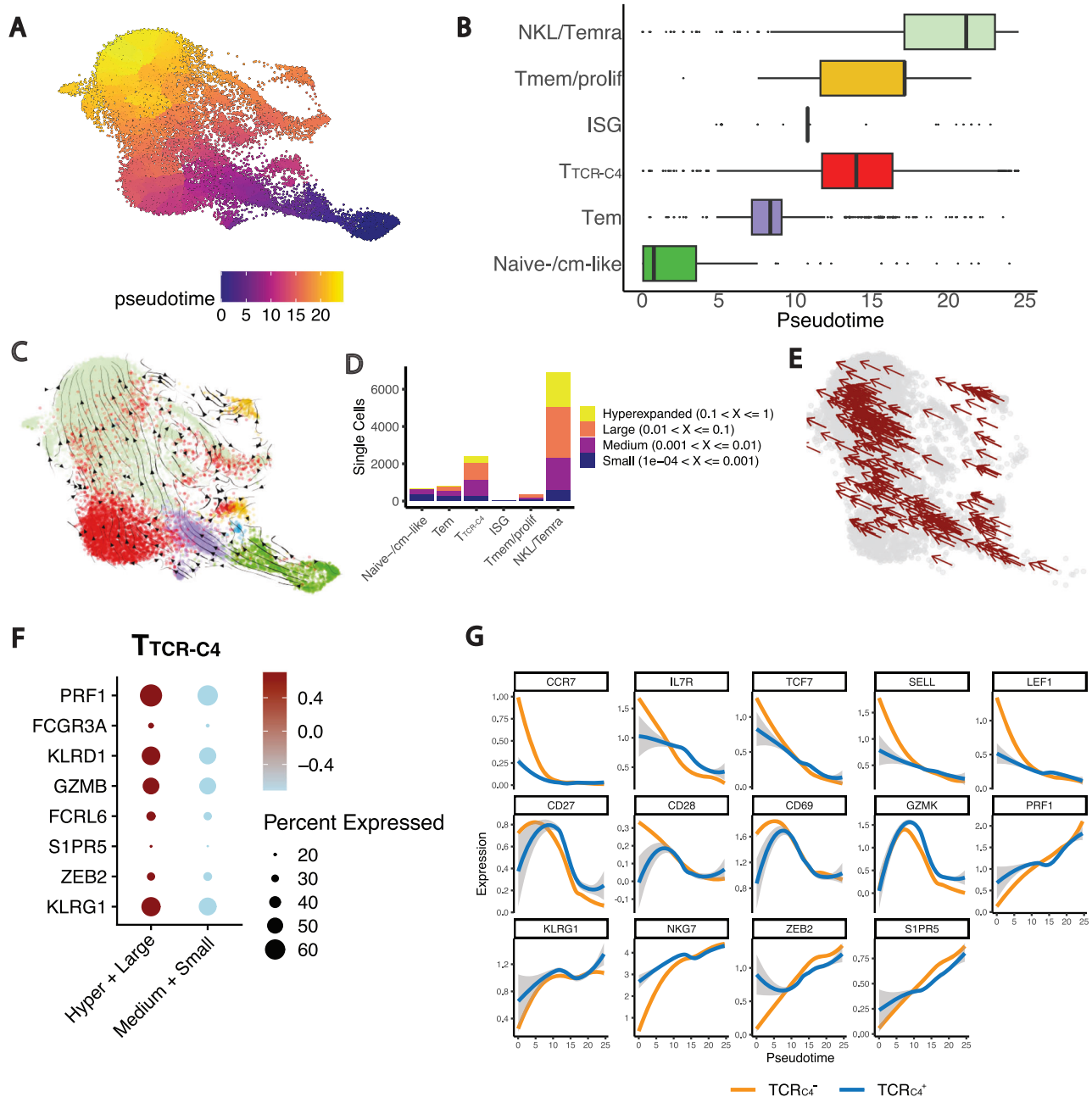
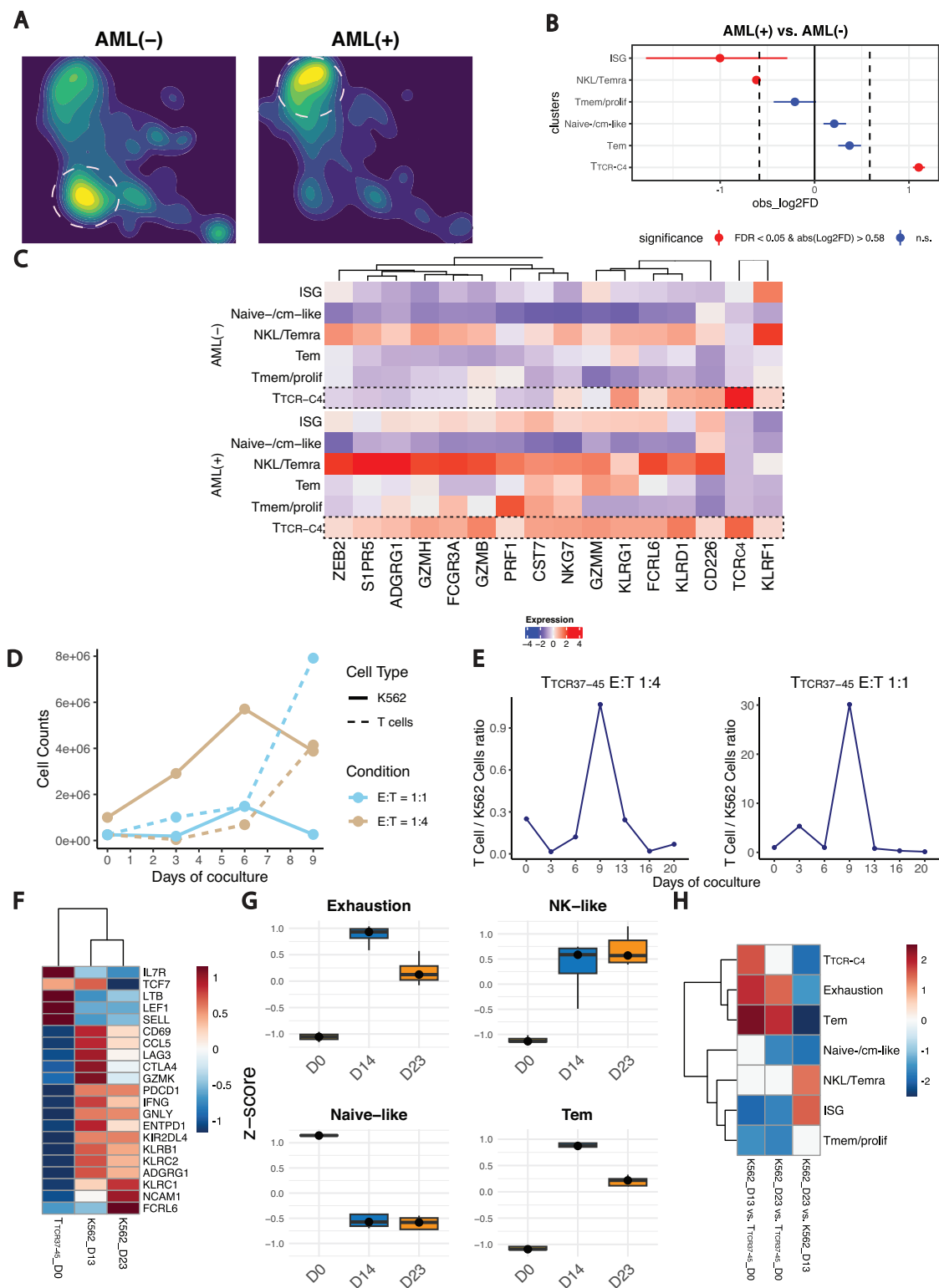


Fig. 4 | CD8⁺ T-cell differentiation dynamics and clonal expansion. **A** UMAP plot illustrating the developmental trajectory of CD8⁺ T-cell transcriptional states, as predicted by Monocle. The color scale represents the pseudotime, where blue indicates earlier developmental stages and orange/yellow indicates later stages. **B** Boxplots showing the distribution of the 5 CD8⁺ T-cell subsets (y-axis) along the pseudotime (x-axis). The position of the boxes provides context for how the subsets are positioned within the developmental trajectory, with subsets at lower pseudotime values representing earlier stages of differentiation, while those at higher pseudotime values correspond to later stages. Boxplots show the IQR; lines denote medians. The bounds of the box represent the 25th and 75th percentiles; whiskers span 1.5x IQR. **C** UMAP plot colored by the annotated CD8⁺ subsets overlaid with the predicted velocity stream computed through scVelo. The velocity streams represent the predicted direction and magnitude of gene expression changes for each individual cell, providing insights into the dynamic transitions between cellular states. These streams highlight the likely trajectories cells follow as

they evolve over time, offering a predictive view of future cellular states based on current transcriptional dynamics. **D** Stacked bar plot showing cell count of different T-cell states (x-axis) in specific clonal frequency ranges. Colors indicate the clonal frequencies. **E** UMAP visualization of hyperexpanded and large CD8⁺ T cell clones, defined in (D), showing shared TCR sequences across different clusters. Each point represents a single cell, while arrows indicate the inferred directionality of clonal expansion across clusters. **F** Dot plot showing the expression of NKL genes in T_{TCR-C4} with a higher degree of clonal expansion (Hyperexpanded, large) vs. less clonally expanded T_{TCR-C4} (Medium, small). Clonal frequency ranges are defined in (D). **G** Line plots displaying the smoothed gene expression of selected genes along the pseudotime for TCR_{C4}⁻ (orange) and TCR_{C4}⁺ (blue) cells. These plots illustrate the dynamic changes in gene expression (y-axis) as cells progress along the inferred trajectory (x-axis). The smoothed curves show how the expression of each gene varies at different pseudotime points.



identified T-cell characteristics associated with AML control in one case.

The characteristics of substrate cells from which T cell products are derived can impact post-transfer persistence. In murine and macaque models, antigen-specific Tcm-like CD8⁺ T cells persist long-term post-adoptive transfer, unlike Temra-like cells^{30,57}. In our study, T_{TCR-C4} generated from EBV-specific CD8⁺ T cells persisted longer

compared to CMV-specific substrate cells which may reflect the distinct biology of EBV and CMV^{58,59}. CMV reactivates periodically, requiring rapidly activated responses that promote Temra differentiation^{60,61}, while EBV tends to remain quiescent, preserving Tcm phenotypes⁶²⁻⁶⁴. While reactivation frequency plays a role, the reactivation microenvironment is also critical. CMV reactivates in non-professional antigen-presenting cells, including fibroblasts, which lack

Fig. 5 | AML induces T_{TCR-C4} NKL/Temra differentiation skewing. **A** UMAP plot of $CD8^+$ T cells colored by density and split by group (AML(-) and AML(+)). AML(+) samples are those with detectable leukemic cells in BM or PB, while AML(-) lack detectable disease. Color intensity reflects $CD8^+$ T-cell density (blue = low, yellow = high). Dashed lines highlight areas of highest density in each group. **B** Point-range plot showing the pairwise (AML(+) vs. AML(-)) proportional difference for each $CD8^+$ T-cell subset. Horizontal lines extending from each point denote the 95% confidence intervals of the \log_2 FD. Colors indicate the statistical significance (red: $FDR < 0.05$, blue: $FDR \geq 0.05$); vertical dashed lines mark the absolute value of \log_2 FD cutoff for significance. **C** Heatmap displaying DGE of NKL genes across the $CD8^+$ T-cell subsets in AML(-) vs. AML(+) (blue = low, red = high expression). Dashed boxes highlight NKL/Temra genes. **D** Line plots showing the absolute cell counts over time (days of coculture) for $T_{TCR37-45}$ (dashed lines) and K562 cells (solid lines) at E:T ratios of 1:1 (sky blue) and 1:4 (tan). **E** Line plots showing the T-cell-to-tumor cell ratio over time for each E:T condition (left: 1:4; right: 1:1). Cell ratios were

calculated based on flow cytometry data. **F** Heatmap depicting significant DEGs across $T_{TCR37-45_DO}$ ($T_{TCR37-45}$ -only), K562_D13 ($T_{TCR37-45}$ T cells after 13 days of coculture with K562 AML cell line), K562_D23 ($T_{TCR37-45}$ T cells after 23 days of coculture with K562 AML cell line) conditions. Significance was determined using DESeq2 ($FDR < 0.05$). Blue = low, red = high expression. **G** Boxplots illustrating the z-score of Exhaustion, NK-like, Naïve-like and Tem signatures across co-culture timepoints. Each box represents the distribution of z-scores for the genes in the respective signature at each timepoint. The center line indicates the median; the box limits represents the IQR, and the whiskers span $1.5 \times IQR$. **H** Heatmap illustrating the enrichment of the top 50 DEGs from scRNAseq-derived subsets (T_{TCR-C4} , Tem, Naïve/cm-like, NKL/Temra, ISG, Tmem/prolif) and manually curated exhaustion markers across three comparisons: K562_D13 vs. $T_{TCR37-45_DO}$, K562_D23 vs. $T_{TCR37-45_DO}$, K562_D23 vs. K562_D13. Red = high, blue = low enrichment. $T_{TCR37-45}$ represents the baseline ($T_{TCR37-45}$ -only condition).

co-stimulatory signals and favor Temra differentiation, whereas EBV reactivates in B cells in lymphoid tissues, providing co-stimulation that may preserve the Tcm phenotype^{65,66}. Our analysis of an independent mass-cytometry dataset³¹ confirmed that EBV-specific cells better maintain self-renewing features than CMV-specific cells. Taken together these findings establish that self-renewal capacity may predict the potential for prolonged T-cell persistence³⁰. However, EBV-specific T_{TCR-C4} were unable to sustain long-term responses in all patients, suggesting additional influences by non-intrinsic AML-related factors.

Despite efforts to investigate T-cell dysfunction in AML^{23,24,50}, several critical questions have remained unanswered²⁷, mainly due to the challenge of identifying AML-specific T cells. In this study, infused T_{TCR-C4} offered the possibility of examining AML-specific T cells and AML biology. We found that T-cell exhaustion is not the primary cause of AML-specific T-cell dysfunction. Instead, T_{TCR-C4} expressing exhaustion markers (PD1, TIGIT, Tim3) also expressed markers of activation (CD38, CD69) and proliferation (Ki67), indicating an effector-like T-cell state. We found that AML-exposed T cells follow a differentiation trajectory from effector-memory to NKL cells, which was associated with compromised T_{TCR-C4} cell persistence and function. These findings are supported by previous works highlighting the importance of T-cell senescence and NKL transition, in addition to exhaustion, as potential mechanisms underlying CAR-T cells dysfunction^{26,40}.

AML's distinct properties, including myeloid cell origin and immunosuppressive effects⁶⁷ via production of reactive oxygen species and other soluble factors, may distinctly redirect T cells toward functional impairment that precludes transitioning to a classical exhausted phenotype and explain the observed NKL skewing in T_{TCR-C4} and endogenous $CD8^+$ T cells. The absence of classical exhausted cells in AML has several implications. In solid tumors, chronic antigen stimulation induces a multi-step epigenetic shift of $CD8^+$ T cells into an exhaustion state⁶⁸, starting from PDI⁺TCF1⁺ precursor/progenitor exhausted cells, whose frequency correlates with response to checkpoint inhibitors⁶⁹. In contrast, our AML findings suggest that the expression of common activation/exhaustion markers reflect recent T-cell activation rather than true exhaustion, which may also explain the limited efficacy of checkpoint inhibitors in AML^{23,50,70,71}. The presence of a distinct dysfunctional program supports the need for new immunotherapy strategies to enhance the efficacy of anti-AML adoptive T-cell therapy to prevent T-cell dysfunction. For example, knocking out ID3 and SOX4 transcription factors in chimeric antigen receptor-engineered (CAR)-T cells in vitro reduces NKL skewing and enhances effector functions²⁶. Whether these strategies can improve cell therapy in AML in vivo remains to be determined.

Contrary to a previous report³⁶, we did not detect serum cytokine changes linked to NK-like skewing. This may reflect the limited sensitivity of serum cytokine levels in capturing T_{TCR-C4} effects within the tumor microenvironment, compared to the pronounced systemic

effects of CAR-T cells. Indeed, CAR-T cells in AML carries a higher incidence of CRS⁷² compared to TCR-T cells¹³.

A potential strategy to reduce NKL skewing of T_{TCR-C4} , as suggested by the outcome in one of our treated patients, could involve the use of the hypomethylating agent azacitidine. While azacitidine has direct anti-leukemia effects⁷³, the prolonged disease control observed in our patient was unusual and prompted further investigation into the underlying mechanisms. Azacitidine administration correlated with clonal expansion and persistence of central memory, as opposed to NKL differentiated T_{TCR-C4} , leading to a prolonged equilibrium between anti-leukemic T_{TCR-C4} and AML MRD. In support of this, a previous study investigating azacitidine combined with nivolumab in AML patients relapsed post-HCT⁷⁴ showed that following the interruption of azacitidine and the initiation of nivolumab, $CD8^+CD57^+KLRG1^+$ T cells significantly increased over time in non-responders. In our study, uninterrupted administration of azacitidine reduced the skewing in NKL (in vivo) and $CD57^+KLRG1^+$ (in vitro) $CD8^+$ T cells, suggesting that a prolonged treatment with azacitidine in addition to having anti-leukemic activity may be beneficial to avoid terminal differentiation and support T_{TCR-C4} persistence. Other studies have also shown that azacitidine can have a negative effect on T regulatory cells⁷⁵, and enhance CAR-T cell activity towards AML⁷⁶. Additionally, in our patient, before receiving the first T-cell infusion, the low WT1 expression in the residual AML likely did not activate T_{TCR-C4} , causing near disappearance of the T cells. However, after azacitidine introduction, T_{TCR-C4} frequencies increased, likely driven by azacitidine-induced WT1 expression⁷⁷. Intermittent T_{TCR-C4} activation by transient induction of WT1 presentation on AML cells by cycles of azacitidine with subsequent temporary clearance of AML may have helped sustain T_{TCR-C4} persistence and response to stimulation. Although further investigation is needed to determine if azacitidine acts preferentially on leukemia cells by increasing WT1 expression, thereby promoting antigen-recognition, and/or T_{TCR-C4} effector functions, these results support evaluating azacitidine as a favorable adjunct to T-cell immunotherapy.

Paradoxically, our ability to track dysfunction was limited to patients with persisting T_{TCR-C4} , in whom T cells remained relatively functional. We hypothesize that patients with more aggressive disease experience accelerated T-cell dysfunction and death rather than establishment of progenitor cells capable of self-renewal; however we were unable to formally test this in our study. Despite a limited sample size, our findings on the nature of T-cell dysfunction in AML were confirmed in larger cohorts of endogenous $CD8^+$ T cells. Additionally, our interpretation of azacitidine's effect on T_{TCR-C4} is based on a single patient and thus should be viewed as preliminary.

In our study, most of the described patients did not undergo lymphodepletion prior to T cell infusions, as this was introduced into the trial only after the safety of T_{TCR-C4} was established. Lymphodepletion could potentially favor cell product expansion and persistence⁷⁸. However, of the three patients who did receive

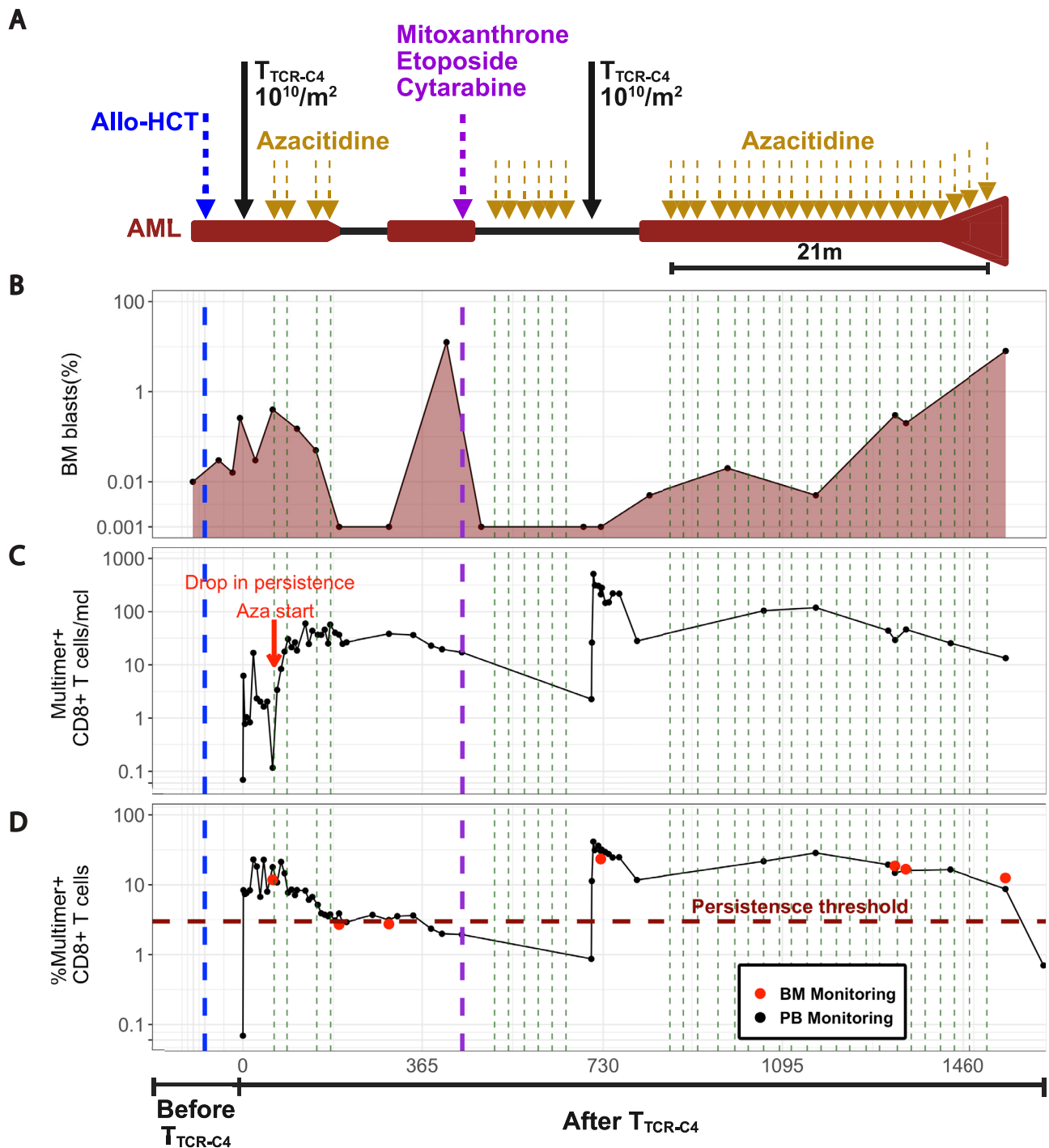


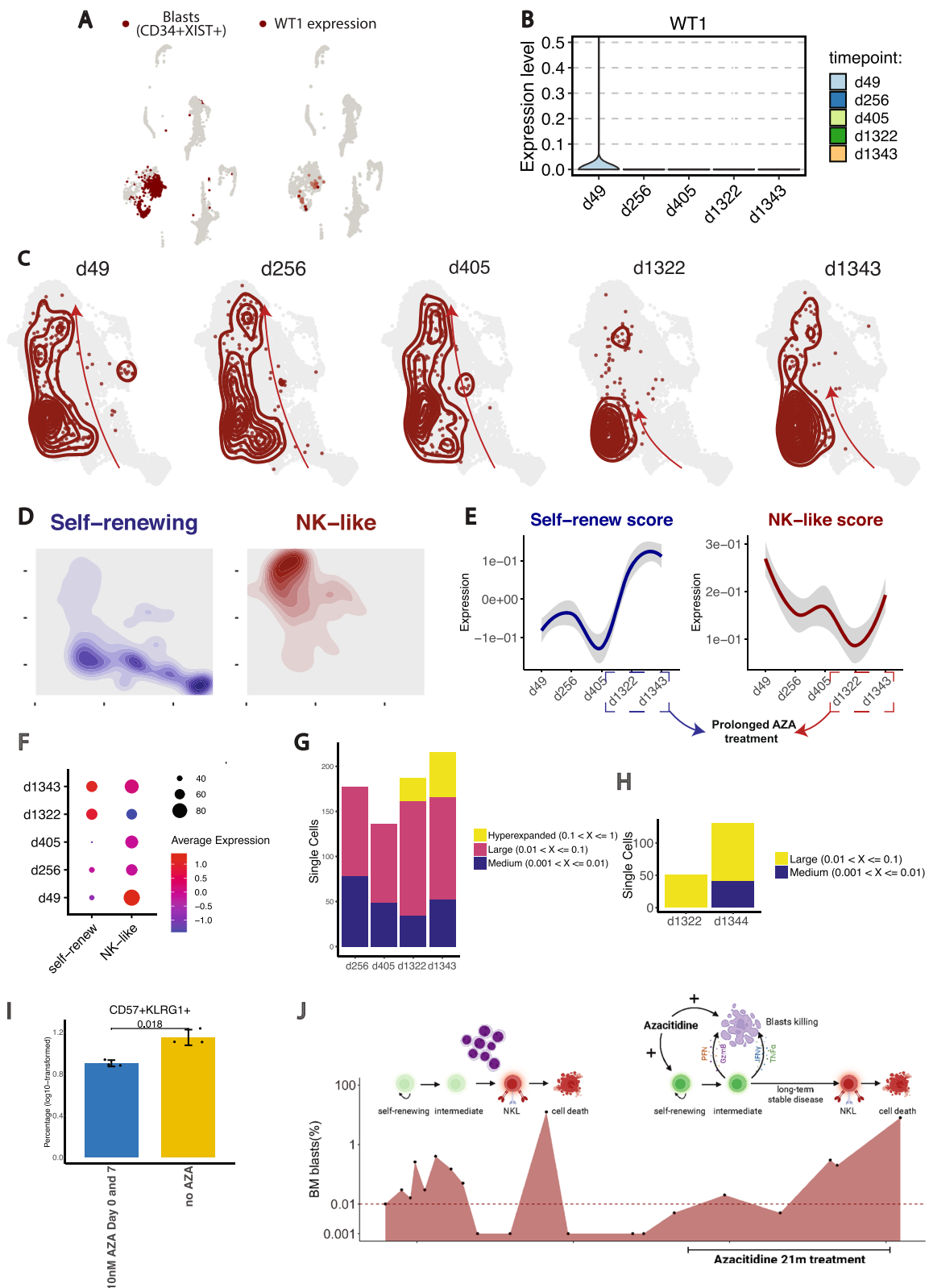
Fig. 6 | Timeline and disease response in a patient with relapsed AML post-allogeneic HCT treated with $T_{\text{TCR-C4}}$ and Azacitidine. A Timeline of patient's treatment regimen. Dark red highlights timeframes with detectable BM AML. **B** Percent of BM AML blasts (y-axis, log scale) by multiparametric flow cytometry

(MFC) at specific timepoints (black dots, dark red shaded area). **C** Multimer⁺ cells/ μl and **D** Percent multimer⁺ of CD8⁺ T cells in PB (black dots) and BM (red dots) collected before and after $T_{\text{TCR-C4}}$ infusions. The red arrow indicates the lack of $T_{\text{TCR-C4}}$ persistence before the start of Azacitidine.

lymphodepletion in this study, only one demonstrated long-term $T_{\text{TCR-C4}}$ persistence. In the prophylactic setting of our previously reported trial¹³, no patient underwent lymphodepletion, yet all patients experienced sustained remissions. These findings suggest that the efficacy of $T_{\text{TCR-C4}}$ may be influenced more by post-HCT AML status rather than preceding lymphodepletion.

Further validation in larger, randomized trials will be needed to confirm and better define the mechanisms of AML-induced T-

cell dysfunction and to clarify whether the limited efficacy of $T_{\text{TCR-C4}}$ in this study reflects an insufficient therapeutic effect of WT1 targeting in active disease or whether cellular therapies are generally less effective in this setting compared to the prophylactic context¹³. However, our study does illuminate some of the complex mechanisms underlying AML-induced T-cell dysfunction and strengthens support for a distinct pathway outside the traditional paradigm of T-cell exhaustion, emphasizing the need to



address this unique dysfunction in future immunotherapy strategies.

Methods

Clinical protocol

The trial was approved by the Fred Hutchinson Cancer Center (FHCC) Institutional Review Board, the US Food and Drug Administration and

the National Institutes of Health Recombinant DNA Advisory Committee. The study was conducted in accordance with the Declaration of Helsinki and was registered at ClinicalTrials.org under the identifier [NCT01640301](https://clinicaltrials.gov/ct2/show/study/NCT01640301) on July 13, 2012. All participants and donors provided written informed consent prior to enrollment. Eligible participants included ‘high-risk’ AML patients with relapsed or refractory disease (overt or MRD) post-HCT along with their fully HLA-matched (10 of 10)

Fig. 7 | Longitudinal single-cell analysis of T_{TCR-C4} transcriptional skewing and clonal evolution in a patient with relapsed AML post-allogeneic HCT. A UMAP plots showing a blast score calculated from *CD34* and *XIST* (female-specific) co-expression in a patient treated with a sex-mismatched transplant (female patient, male donor), along with *WT1* expression. Cells with high scores are in dark red. **B** Violin plot of the *WT1* expression across timepoints post- T_{TCR-C4} infusion (d49, d256, d405, d1322, d1343). **C** UMAP plots of PB $CD8^+$ T cells from the scRNAseq dataset, with the T_{TCR-C4} subset from patient 8 highlighted (dark red). Kernel density contours depict the density of T_{TCR-C4} cells within the $CD8^+$ T cell landscape at each timepoint (d49, d256, d405, d1322, and d1343). Arrows were added manually to indicate the different skewing of T_{TCR-C4} across the timepoints examined. **D** UMAP plots of PB $CD8^+$ T cells, with density contours highlighting cells with high (above 75th percentile) self-renewing (*TCF7*, *LEF1*, *SELL*, *CCR7*, *BCL2*, *IL7R*, *CD27*, *CD28*; blue) and NK-like (*ZEB2*, *SIPRS*, *CX3CR1*, *KLRG1*, *NKG7*, *FCRL6*, *KLRD1*, *ADGRG1*; red) gene scores. **E** Line plots showing the temporal changes in the self-renew (left) and NK-like (right) scores of T_{TCR-C4} . The blue (self-renew) and dark red

(NK-like) lines represent LOESS-smoothed means of the scores, with shaded areas indicating the 95% confidence interval. The y-axis reflects score expression values. **F** Dot plot showing the self-renew and NK-like scores of T_{TCR-C4} across timepoints post-infusion. **G** Stacked bar plot showing cell count of PB T_{TCR-C4} within specific clonal frequency ranges over time (d256, d405, d1322, d1343). Colors indicate the clonal frequencies. **H** Stacked bar plot showing cell count of BM T_{TCR-C4} within specific clonal frequency ranges at d1322 and d1343. Colors indicate the clonal frequencies. **I** Bar plot illustrating the log₁₀-transformed percentage of $CD57^+KLRG1^+$ T_{TCR-C4} after CD3/CD28 stimulation \pm 10 nM AZA. Data are presented as mean \pm standard deviation ($n = 6$, 3 biological replicates/condition). Two-sided Welch's t-test was used for statistical testing, assuming unequal variances between groups. **J** Cartoon showing the influence of blasts and azacitidine on T_{TCR-C4} . The red area under the curve represents the blasts percentage over time. Blasts induce T_{TCR-C4} skewing towards NK-like and cell death; azacitidine supports self-renewal and long-term persistence. Created in BioRender. Mazziotta, F. (<https://BioRender.com/twt3jx5>).

related or unrelated donors expressing HLA A*0201 (HLA-A2). The primary endpoints were safety and toxicity, assessed by the nature and severity of adverse events related to the study treatment, and disease response, evaluated in patients with active disease (MRD or overt relapse). Secondary endpoints included the persistence and migration of transferred T cells to the bone marrow, the maintenance of TCR expression and function in transduced T cells, and clinical outcomes following T-cell therapy.

Patient selection

HLA-A2 genotype was confirmed by high-resolution typing before enrollment. Exclusion criteria included: refractory central nervous system disease, HIV seropositivity, grade ≥ 3 GVHD and no available CMV/EBV-seropositive matched donor. The sample size for this study was not based on formal power calculations, but on feasibility, the potential to provide descriptive information, determine whether further study was warranted and evaluate toxicity. Sex and age were not considered in the study design due to the sample size and the exploratory nature of the study. Accordingly, no sex- or age-based analyses were performed. The sex and age of participants were recorded based on clinical documentation and are reported in aggregate. Consent to specifically report or share individual-level data, that could potentially identify the patients based on age, sex, institution of treatment and disease was not obtained. Participants were not compensated for their participation in this study. The first participant was enrolled on April 29, 2013 and the last participant was enrolled on February 1, 2019.

Treatment plan

Isolation of TCR_{C4} , lentiviral vector construction, and T_{TCR-C4} generation were performed as previously described¹³. Patients were eligible to receive a first infusion of T_{TCR-C4} after demonstrating relapse (overt or MRD) at any time post allogeneic HCT. Patients 26, 27, 28 received lymphodepleting treatment before the first T_{TCR-C4} infusion with cyclophosphamide (300 mg/m² IV) and fludarabine phosphate (30 mg/m² IV) daily on days -4 to -2. Patients 1, 2, 4, 5, 6, 7, 8, 9 received four escalating doses of T_{TCR-C4} (patient 3 received the cells on Arm 1) starting at 10^9 cells per m² on day 0, then 3.3×10^9 cells per m² on day 14 and 10^{10} cells per m² on days 28 and 42. followed by low-dose subcutaneous IL-2 (2.5×10^5 IU twice daily) for 14 d (stage 1) administered to enhance the survival of transferred T cells. After safety was established, the remaining 7 patients received 2 doses of 10^{10} cells per m² on day 0 and on day 28 followed by 14 days of low-dose subcutaneous IL-2. A second T_{TCR-C4} infusion was administered only if the frequency of T_{TCR-C4} was $<3\%$ of total peripheral $CD8^+$ T cells. Patients 5, 7, 19, 23, 27 received 1 infusion, patients 4, 8, 14, 15, 26, 28 received 2 infusions, patient 1 received 3 infusions, the remainder received 4 infusions (Table 1). Patients were monitored for toxicities, based on Common

Toxicity Criteria v4.0. Treatment was declared safe based on the toxicity rate ($< 30\%$). Non-hematologic toxicity requiring treatment discontinuation was defined as any grade 3 or 4 non-hematologic toxicity (CTCAE 4) that was deemed to be caused by infusion of the study treatment. Hematologic toxicity requiring treatment discontinuation (blood/bone marrow CTCAE 4) was defined as any new or recurrent onset of grade 4 hematologic toxicity that occurred after the first T cell infusion, and lasted for two consecutive days, and was attributed to any other identifiable cause other than T cell infusion. Exceptions included grade 4 lymphopenia if it returned to pre-infusion levels within 14 days, as a transient drop in lymphocyte counts was expected after T cell infusions, and platelet counts $< 20,000/\text{mm}^3$, which are common in this post-HCT population.

Assessment of disease status

Morphology, multiparameter flow cytometry, standard cytogenetics or genomic technologies were routinely performed on bone marrow aspirates and peripheral blood samples that were obtained from all patients. Any level of residual disease was considered to indicate positivity for MRD.

T cell tracking by WT1 peptide/HLA (pHLA) tetramers

WT1 pHLA-specific tetramers (produced by the FHCC Immune Monitoring Core Facility) were used to detect T_{TCR-C4} in PBMCs collected after infusions, with a staining sensitivity of 0.01% of total $CD8^+$ T cells, as previously described¹³. T_{TCR-C4} percentages were calculated using FlowJo v.10 (Treestar).

Patient outcomes and survival analysis

Kaplan-Meier OS curves were estimated using the *survminer* (v0.4.9) and *survival* (v3.3-1) packages in R. OS was calculated from the date of first T_{TCR-C4} infusion to the date of death or censoring. Outcomes of responding patients were represented using a swimmer plot. Day 0 was defined as the post-HCT relapse date or, for HCT-refractory patients, as day 28 post-HCT, at which timepoint persistent disease was observed. R package *swimplot* (v1.2.0) was used for visualization.

Analysis of T_{TCR-C4} persistence

Persistence of TCR-T cells ($\%T_{TCR-C4}$) over time was visualized using *ggplot2* (v3.4.4) R package. Wilcoxon rank-sum tests were used for pairwise comparisons between T_{TCR-C4} with different virus-specificity (EBV vs. CMV) over time. Kruskal-Wallis tests were applied for multi-group comparisons.

Fisher's exact test was used to evaluate the association between disease risk and T_{TCR-C4} persistence. The test was chosen due to the small sample size and binary classification of persistence (long-term vs. short-term) and disease risk (disease +/early post-HCT relapse vs. MRD-/non early post-HCT relapse). Statistical significance was

assessed with a p -value threshold of 0.05. One patient was excluded from this analysis due to the unavailability of WT1-expression data, which could confound interpretation of the persistence results.

To correlate quantitative parameters before infusion with T_{TCR-C4} persistence we used first a logistic regression model to evaluate the association between persistence and absolute white blood cells, neutrophils, lymphocytes, monocytes, eosinophils, basophils, and blasts percentage. Next, we fit lasso regression using the *glmnet* R package to identify key predictors of persistence. Cross-validation was performed to determine the optimal lambda parameter, and model coefficients were extracted at the optimal penalty value.

Flow-cytometry

Cryopreserved PBMCs were thawed and allowed to rest overnight in RPMI medium supplemented with 10% fetal bovine serum (R10). The cells underwent stimulation with a cocktail containing the WT1₁₂₆₋₁₃₄ peptide at a final concentration of 1 µg/ml in R10 and intracellular cytokine staining, as previously described¹³. Flow cytometry was conducted on an LSRII instrument (Becton Dickinson) with data acquisition using FACS-Diva software v.8.0.1. Flow cytometry data were subsequently analyzed using FlowJo v.10 (Treestar).

To test the overall decline of IFN γ production over time in T_{TCR-C4} (tetramer positive) cells and account for repeated measures from the same subjects, we employed a linear mixed-effects model using the lmer function from the lmerTest package. This model included Timepoint as a fixed effect and subject IDs as a random effect. To ensure the appropriate distribution for analysis, the percentage values were log-transformed (using log₁₀) to stabilize variance and normalize the data. We modeled the relationship between log₁₀-transformed percentages of tetramer positive IFN γ -producing cells and the Timepoint factor, with T0 serving as the reference level (intercept) for comparison.

The full formula used to fit the model was: lmer(Tet.pos_IFN γ ~ Timepoint + (1 | id), data = df), where Tet.pos_IFN γ represents the log₁₀-transformed percentages of tetramer positive IFN γ -producing cells, Timepoint is the timepoint, id is the subject IDs, and df is the dataset employed (Supplementary table 6). All statistical analyses were conducted using R (v4.3.2), with results considered significant at $p < 0.05$.

Spectral flow cytometry

Post-infusion PB samples were analyzed using a 5-laser Cytek Aurora. Antibodies used are listed in Supplementary Table 4. T_{TCR-C4} were identified by binding to the APC dye-labeled HLA-A2:WT1₁₂₆₋₁₃₄ tetramer. Spectral flow-cytometry data were biexponentially transformed, compensated and preprocessed (aggregates and dead cell removal) in FlowJo V10 (TreeStar). Pregated CD8⁺ T cells were exported from FlowJo and loaded in R (v4.3.2). First we created a flowSet using *flowCore* (v2.12.2)⁷⁹ and subsequently analyzed the data using *CATALYST* (v1.24.0)⁸⁰.

Ki67 was then used to manually gate subsets of interest using the FlowJo software. Statistical analysis included Kruskal-Wallis to compare T_{TCR-C4_Temra} and T_{TCR-C4_Tem} percentages over time, and Wilcoxon rank-sum test for comparing KLRG1⁺CD57⁺GNLY⁺ and Tim3⁺PDI⁺TIGIT⁺ T_{TCR-C4_Temra} .

In silico mass cytometry validation

Mass cytometry files used to generate an atlas of virus-specific CD8⁺ T cells³¹ were downloaded from (<https://zenodo.org/records/8330231>). Data were analyzed using *flowCore* and *CATALYST* R packages as specified above.

Serum cytokine analysis

Quantitative cytokine analysis was performed at our institution using a Luminex-based multiplex immunoassay. Serum samples were collected, processed, and stored at -80 °C prior to analysis. Cytokine

concentrations were measured using a Luminex instrument following the manufacturer's protocols. Results were reported as concentration values (pg/mL). Statistical analysis was performed in R (v4.3.2), with the Wilcoxon rank-sum test used for pairwise comparisons between timepoints and the Kruskal-Wallis test applied to study the overall concentration changes over time.

Single Cell RNA Sequencing

Patients with $T_{TCR-C4} \geq 3\%$ of the total CD8⁺ T cells at day 28 or later after first infusion were selected for scRNAseq analysis. Available PBMCs or BMMCs were thawed, washed and loaded on a 10x Chromium Controller based on the 3' Chromium or 5' Chromium Single Cell V(D)J Reagent Kit manual (10x Genomics). Library preparation was performed as per manufacturer's protocol with no modifications. Library quality was confirmed by TapeStation High Sensitivity (Agilent, evaluates library size), Qubit (Thermo Fisher, evaluates dsDNA quantity), and KAPA qPCR analysis (KAPA Biosystems, evaluates quantity of amplifiable transcript). Samples were mixed in equimolar fashion and sequenced on an Illumina HiSeq 2500 rapid run mode according to the standard 10X Genomics protocol. TCR target enrichment, 5' gene expression library, and TCR library were carried out according to the 5' Chromium Single Cell V(D)J Reagent Kit manual (10x Genomics). The 10X Genomics software Cell Ranger (v2.0.0) was used to process the raw data FASTAQ files with default parameters. The EmptyDrops method⁸¹ was used to identify cells with low RNA contents. The "count" function was used to perform alignment, filtering, barcode counting and UMI counting. Reads were aligned to the hg38 human reference genome (Ensembl) and the known transgene codon-optimized sequence using Spliced Transcripts Alignment to a Reference (STAR)⁸².

For V(D)J sequencing assembly and paired clonotype calling, we used CellRanger "vdj" function. This function leverages Chromium cellular barcodes and UMIs to assemble V(D)J transcripts for each cell. CellRanger V(D)J calling produces an output named "filtered_contig_annotations.csv" for each sample, which lists CDR3 amino acid and nucleotide sequences for single cells identified by their barcodes.

scRNAseq quality control and subsetting

The filtered feature matrices generated by the CellRanger pipeline were used for downstream quality control (QC) and analyses. We used the function read10xCounts from the R package *DropletUtils* (version 1.14.2) to load the CellRanger output in R as a SingleCellExperiment⁸³ object. Doublet cells filtering was performed on each sample using the *scds* package (v1.10.0)⁸⁴. QC and filtering were conducted using the *scater* R package (v1.22.0)⁸⁵. Genes with zero counts across all cells were removed from the analysis. This was achieved by filtering out genes that had no detected expression in any cell (row sums of counts equal to zero). Cells were filtered based on feature counts, the percentage of mitochondrial and ribosomal genes, and the number of expressed features. Cells with values beyond a specific threshold, between 1 and 3.5 median absolute deviations (MAD) from the median, were excluded. These MAD thresholds were established according to the quality of each sample. Features with a count greater than 1 in at least 3 cells were retained for downstream analysis. We then split cells by sample in 15 datasets, normalized, found the 2000 most variable genes and scaled for each dataset using *Seurat* (v4.3.0.9001) SplitObject, NormalizeData, FindVariableFeatures and ScaleData respectively^{86,87}. For batch correction, we used the FindIntegrationAnchors and IntegrateData functions from *Seurat*. The integrated dataset was then used for scaling (ScaleData) and dimensionality reduction (PCA and UMAP) using RunPCA and RunUMAP, respectively. UMAP dimension reduction and clustering were computed using the first 20 principal components (PCs). The number of PCs capturing most of the variation in our data was selected using *Seurat* function ElbowPlot which visualizes the standard deviation of

each PC. Clusters were identified via shared-nearest-neighbor-based (SNN) clustering and further analyzed at a resolution of 0.6. To assess whether NK cells were depleted after $T_{\text{TCR-C4}}$ infusion, we used the scGate tool³⁷ to identify NK cells as positive for *NCAM1*, *KLRD1*, *KLRG1*, and negative for *CD3D*, *CD3G*. NK cells constituted ~10% of total peripheral blood cells, indicating no significant depletion. $CD8^+$ cell subset was identified using scGate (v1.0.1) and subsequently extracted with Seurat subset function.

scRNAseq $CD8^+$ endogenous and $T_{\text{TCR-C4}}$ analysis

The $CD8^+$ subset was used to find the 2000 most variable features (FindVariableFeatures), scale the data (ScaleData), and run dimensionality reduction (runPCA and runUMAP). SNN was used for clustering with a resolution of 0.5 for downstream analysis. Differential gene expression across and between clusters or condition (e.g. AML(+) vs AML(-)) was computed using Seurat FindMarkers and FindAllMarkers with default parameters. TCR_{C4} -transgene⁺ cells were identified using scGate (v1.0.1). For visualization purposes, we used Seurat built-in functions alongside *ComplexHeatmap* (v2.15.1)⁸⁸, *scCustomize* (v1.1.0.9001) (<https://github.com/samuel-marsh/scCustomize>) and *SCP* (<https://github.com/zhanghao-njmu/SCP>). The pan-cancer $CD8^+$ single-cell reference atlas was built using the *CD8.thisStudy_10X.seu.rds* file⁴¹ downloaded from Zenodo and processed using the *make.reference* function from the *ProjecTILs* R package (v3.2.0)⁸⁹. We then used Run.Projectils function, from the same package, to project the cell states from the query dataset onto the reference.

Cell trajectory inference was computed using the *Monocle*⁴⁵ R package (v1.3.4), with UMAP used as dimensionality reduction. Single-gene expression patterns along the pseudotime were visualized using the *plot_genes_in_pseudotime* function in *Monocle*. RNA velocity was conducted by exporting the $CD8^+$ T-cell Seurat object as an h5ad file using the R package *seurat-disk* (v0.0.0.9020) (<https://github.com/mojaveazure/seurat-disk>), loading this file in Python (v3.8.14) as AnnData object⁹⁰, and estimating velocities with the *scvelo* Python package (v0.2.4)⁴⁶ using the deterministic model.

We classified patients as AML(+) or AML(-) based on the presence of detectable blasts in BM or PB. Three patients lacked BM or PB evaluations at one timepoint each. For two of these patients, we used the donor-recipient (male-female) sex mismatch. Patient 8 at day 49 exhibited cells expressing the female-specific gene *XIST* alongside the AML-associated genes *CD34* and *WT1* (Supplementary Fig. 18A); similarly, patient 26 expressed *XIST* in a *RPS4Y1* (male-specific gene) negative region at days 7 and 28, thus classified as AML(+) at these timepoints (Supplementary Fig. 18B). Patient 4 was categorized as AML(-) at day 100 and AML(+) at day 581, as previously reported⁴⁹.

To assess the significance of differences in cell proportions per $CD8^+$ cell state between groups (AML(+) vs AML(-)), a permutation test was applied. Specifically, the *permutation_test* and *permutation_plot* functions from the R package *scProportionTest* (version 0.0.0.9000) (<https://github.com/rpolICASTRO/scProportionTest>) were used with default parameters.

For scRNAseq in silico validation, we compiled scRNAseq datasets from independent studies on AML^{23,25,50–52}, lung cancer⁵⁵, pancreatic cancer⁵³ and melanoma⁵⁴. $CD8^+$ T cells were identified and extracted using the *scGate* R package. These cells were then projected onto the pan-cancer $CD8^+$ T cell reference atlas⁴¹ using *ProjecTILs* R package.

Signatures of T-cell dysfunction^{25,47,48} and KLR-exhaustion^{42,43}, were scored and integrated into our $CD8^+$ T-cell Seurat object using Seurat's AddModuleScore. These signatures were then projected onto the $CD8^+$ two-dimensional UMAP or visualized using DotPlot in Seurat to assess expression patterns.

To assess changes in TCR-signaling as $T_{\text{TCR-C4}}$ undergo NK-like skewing, we first identified the NKL $T_{\text{TCR-C4}}$ and the non-NKL $T_{\text{TCR-C4}}$. This was achieved by extracting the UMAP coordinates of $T_{\text{TCR-C4}}$ and

endogenous NKL/Temra and computing pairwise Euclidean distances between them. Cells within a defined threshold distance (0.1) were considered overlapping. $T_{\text{TCR-C4}}$ overlapping with endogenous NKL-Temra were labeled $T_{\text{TCR-C4}}_{\text{NKL}}$ and visualized using Seurat's DimPlot. To identify transcriptional differences between NKL $T_{\text{TCR-C4}}$ and non-NKL $T_{\text{TCR-C4}}$ cells, we performed differential expression analysis using Seurat's FindMarkers. Genes were ranked based on their log fold change and adjusted *p*-values, and GSEA was conducted using *fgsea* (v1.28.0) to evaluate the enrichment in KEGG TCR signaling pathway. To further assess the expression of key TCR signaling genes, we generated dot plots for *CD3D*, *CD3E*, *CD3G*, *LCK*, *ZAP70* and *LAT*. Additionally, we used the KEGG TCR signaling pathway and Seurat's AddModuleScore to compute a TCR signaling score, and then compare its expression between non-NKL $T_{\text{TCR-C4}}$ and NKL $T_{\text{TCR-C4}}$.

The TCR repertoire was analyzed using the R package scRepertoire (v1.10.1)⁹¹. Initially the degree of single cells clonal expansion was defined based on the number of cells sharing the same clonotype. The function *occupiedscRepertoire* was used to visualize the degree of clonal expansion by cell-state over time. To infer clonal trajectories, we first identified hyperexpanded and large clones and mapped them to their respective clusters and UMAP coordinates. We then tracked clones that appeared in multiple clusters, starting from their least abundant state and progressing to their more expanded forms. Finally, centroids for each clone in different clusters were calculated, and directional vectors were generated to infer the movement of these clones.

In vitro chronic antigen stimulation model

The in vitro dysfunction model was established as previously described²⁶. The WT1⁺ K562 tumor cell line (CCL-243, obtained from the ATCC) was transduced with lentiviral constructs to express HLA-A*02:01 and GFP, then sorted for purity using the Sony MA900 cell sorter. Cells were then cultured in media consisting of IMDM with GlutaMAX (Gibco, Life Technologies, #31980030) with 10% FBS, and 1% of penicillin/streptomycin.

$T_{\text{TCR37-45}}$ cells were obtained following previously published protocols⁴⁹. We selected TCR-T cells targeting WT1₃₇₋₄₅ as K562 cell line primarily express the standard proteasome and is not lysed by $T_{\text{TCR-C4}}$ targeting WT1₁₂₆₋₁₃₄⁴⁹. T cells expressing an irrelevant virus-specific TCR were used as negative control. Co-cultures of T cells with K562 cells were established at a 1:1 and 1:4 E:T ratio (2.5×10^5 T cells, 2.5×10^5 or 1×10^6 tumor cells, respectively). After 3-4 days of coculture, 250 μ l of the cell suspension was used for T cell counting and flow-cytometry staining. The remaining cell suspension was spun down, and cells were resuspended in fresh media. A Novocyte 3 lasers flow cytometer was used to quantify GFP⁺ tumor cells and T cells and to maintain constant E:T ratios by reseeding K562 cells. Notably, during the peak of T-cell expansion (day 9–13), the volumes of the cocultures were reduced to ensure the reseeding of an adequate number of tumor cells, thereby maintaining constant E:T ratios. This protocol was followed for 23 days.

Bulk RNA sequencing

Bulk RNA sequencing was performed using BGISEQ-500 platform at BGI Genomics. Briefly, total RNA was extracted using the Qiagen RNeasy Micro Kit according to the manufacturer's instructions. For the construction of low input polyA mRNA-seq libraries, the *SMARTseq* (v4) Package was used. Sequencing was performed on a DNBseq T7 machine (MGI) with paired-end 150 bp reads, generating 30 M raw reads per sample. Raw sequencing data were filtered and trimmed using the software Soapnuke developed by BGI Genomics. The filtered reads were then aligned to the reference transcriptome using *Bowtie2* (v2.2.5). Gene read counts were subsequently generated from the alignment results using *RSEM* (v1.2.8).

To assess differences over time across conditions (T_{TCR37-45_D0}, K562_D14, and K562_D23), we used the likelihood ratio test (LRT) with a full model of -Condition and a reduced model including only the intercept (reduced = - 1). Normalized counts were obtained using the rlog transformation, and differential expression analysis was performed using the R package *DESeq2* (v1.42.0)⁹². We manually curated a list of genes of interest (Supplementary Table 14) and filtered the results to retain only those genes that were significant (padj < 0.05) with an absolute log₂ fold-change > 1). For visualization purposes, average normalized counts of biological replicates were calculated using the *avereps* function from the R package *limma* (v3.56.2) and visualized using the R package *heatmap* (v1.0.12). To visualize the expression patterns of manually curated gene signatures, we calculated z-scores for the averaged normalized counts across conditions (T_{TCR37-45_D0}, K562_D14, and K562_D23). Finally, to compare the enrichment of scRNAseq-derived gene signatures (top 50 differentially expressed genes) and of a manually curated exhaustion signature across conditions, we used the *hciR* (v1.7) function *fgsea_all* with default parameters and *plot_fgsea* for plotting.

In vitro 5-Azacytidine treatment of CD8⁺ T_{TCR-C4} cells

A total of 1×10^6 CD8⁺ T_{TCR-C4} cells were seeded on day 0 and treated with 10 nM or no Azacytidine on days 0 and 7. To activate and drive differentiation of the T cells, T Cell Transact (Miltenyi, 714 130-111-160) was added on days 1 and 8. CD8⁺ T_{TCR-C4} cells were derived from healthy donor PBMCs, and the experiments were performed using independent biological replicates. Flow cytometry analysis was performed on a Symphony A3 715 cytometer at multiple time points: day 0, day 7, and day 14. Data were analyzed using R, where CD57⁺ KLRG1⁺ cell frequencies were log₁₀-transformed and normality was assessed by the Shapiro Wilk test. Statistical analysis (Welch's t-test) and visualization were conducted using the *ggpubr* (v0.6.0.999) package.

Reporting summary

Further information on research design is available in the Nature Portfolio Reporting Summary linked to this article.

Data availability

The gene expression data, including de-identified BAM files and count matrices, generated in this study have been deposited in the NCBI Gene Expression Omnibus (GEO) under accession number [GSE285214](https://www.ncbi.nlm.nih.gov/geo/query/acc.cgi?acc=GSE285214). Previously published mass cytometry data analyzed in this manuscript are available on [Zenodo](https://zenodo.org). Previously published AML scRNAseq data analyzed in this study are available from the European Genome-Phenome Archive (EGA) (<https://ega-archive.org>) under the accession numbers [EGAS00000000357](https://ega-archive.org/accions/EGAS00000000357), [EGAS00001004444](https://ega-archive.org/accions/EGAS00001004444) and [EGAS00001004894](https://ega-archive.org/accions/EGAS00001004894); the NCBI's Database of Genotypes and Phenotypes (dbGaP; <https://www.ncbi.nlm.nih.gov/gap>) under accession number [phs003015.v1.p1](https://www.ncbi.nlm.nih.gov/geo/query/acc.cgi?acc=phs003015.v1.p1); and the GEO repository under accession numbers [GSE128933](https://www.ncbi.nlm.nih.gov/geo/query/acc.cgi?acc=GSE128933) and [GSE185381](https://www.ncbi.nlm.nih.gov/geo/query/acc.cgi?acc=GSE185381). Previously published solid tumor scRNAseq data are available in the GEO repository under accession number [GSE215121](https://www.ncbi.nlm.nih.gov/geo/query/acc.cgi?acc=GSE215121) (melanoma), [GSE148071](https://www.ncbi.nlm.nih.gov/geo/query/acc.cgi?acc=GSE148071) (lung), and [GSE211644](https://www.ncbi.nlm.nih.gov/geo/query/acc.cgi?acc=GSE211644) (pancreas). The remaining data are available within the Supplementary Information, or Source Data file. Source data are provided with this paper.

References

- Bejanyan, N. et al. Survival of patients with acute myeloid leukemia relapsing after allogeneic hematopoietic cell transplantation: a center for international blood and marrow transplant research study. *Biol. Blood Marrow Transpl.* **21**, 454–459 (2015).
- Schmid, C. et al. Treatment, risk factors, and outcome of adults with relapsed AML after reduced intensity conditioning for allogeneic stem cell transplantation. *Blood* **119**, 1599–1606 (2012).
- Webster, J. A., Luznik, L. & Gojo, I. Treatment of AML Relapse After Allo-HCT. *Front Oncol.* **11**, 812207 (2021).
- Cobbold, M. et al. Adoptive transfer of cytomegalovirus-specific CTL to stem cell transplant patients after selection by HLA-peptide tetramers. *J. Exp. Med.* **202**, 379–386 (2005).
- Haque, T. et al. Complete regression of posttransplant lymphoproliferative disease using partially HLA-matched Epstein Barr virus-specific cytotoxic T cells. *Transplantation* **72**, 1399–1402 (2001).
- Schmitt, A. et al. Adoptive transfer and selective reconstitution of streptamer-selected cytomegalovirus-specific CD8⁺ T cells leads to virus clearance in patients after allogeneic peripheral blood stem cell transplantation. *Transfusion* **51**, 591–599 (2011).
- Uhlin, M. et al. A novel haplo-identical adoptive CTL therapy as a treatment for EBV-associated lymphoma after stem cell transplantation. *Cancer Immunol. Immunother.* **59**, 473–477 (2010).
- Cheever, M. A. et al. The prioritization of cancer antigens: a national cancer institute pilot project for the acceleration of translational research. *Clin. Cancer Res.: Off. J. Am. Assoc. Cancer Res.* **15**, 5323–5337 (2009).
- Inoue, K. et al. WT1 as a new prognostic factor and a new marker for the detection of minimal residual disease in acute leukemia. *Blood* **84**, 3071–3079 (1994).
- Menssen, H. D. et al. Presence of Wilms' tumor gene (wt1) transcripts and the WT1 nuclear protein in the majority of human acute leukemias. *Leukemia* **9**, 1060–1067 (1995).
- Miyoshi, Y. et al. High expression of Wilms' tumor suppressor gene predicts poor prognosis in breast cancer patients. *Clin. Cancer Res.: Off. J. Am. Assoc. Cancer Res.* **8**, 1167–1171 (2002).
- Stromnes, I. M., Schmitt, T. M., Chapuis, A. G., Hingorani, S. R. & Greenberg, P. D. Re-adapting T cells for cancer therapy: from mouse models to clinical trials. *Immunol. Rev.* **257**, 145–164 (2014).
- Chapuis, A. G. et al. T cell receptor gene therapy targeting WT1 prevents acute myeloid leukemia relapse post-transplant. *Nat. Med.* **25**, 1064–1072 (2019).
- Kharfan-Dabaja, M. A. et al. Second allogeneic haematopoietic cell transplantation using HLA-matched unrelated versus T-cell replete haploidentical donor and survival in relapsed acute myeloid leukaemia. *Br. J. Haematol.* **193**, 592–601 (2021).
- Kolb, H. J. et al. Graft-versus-leukemia effect of donor lymphocyte transfusions in marrow grafted patients. *Blood* **86**, 2041–2050 (1995).
- Fraietta, J. A. et al. Determinants of response and resistance to CD19 chimeric antigen receptor (CAR) T cell therapy of chronic lymphocytic leukemia. *Nat. Med.* **24**, 563–571 (2018).
- Deng, Q. et al. Characteristics of anti-CD19 CAR T cell infusion products associated with efficacy and toxicity in patients with large B cell lymphomas. *Nat. Med.* **26**, 1878–1887 (2020).
- Kirouac, D. C. et al. Author Correction: Deconvolution of clinical variance in CAR-T cell pharmacology and response. *Nat. Biotechnol.* **41**, 1655 (2023).
- Eyquem, J. et al. Targeting a CAR to the TRAC locus with CRISPR/Cas9 enhances tumour rejection. *Nature* **543**, 113–117 (2017).
- Blank, C. U. et al. Defining 'T cell exhaustion. *Nat. Rev. Immunol.* **19**, 665–674 (2019).
- Grosser, R., Cherkassky, L., Chintala, N. & Adusumilli, P. S. Combination immunotherapy with CAR T cells and checkpoint blockade for the treatment of solid tumors. *Cancer Cell* **36**, 471–482 (2019).
- Hirayama, A. V. et al. Timing of anti-PD-L1 antibody initiation affects efficacy/toxicity of CD19 CAR T-cell therapy for large B-cell lymphoma. *Blood Adv.* **8**, 453–467 (2024).
- Penter, L. et al. Mechanisms of response and resistance to combined decitabine and ipilimumab for advanced myeloid disease. *Blood* **141**, 1817–1830 (2023).

24. Rutella, S. et al. Immune dysfunction signatures predict outcomes and define checkpoint blockade-unresponsive microenvironments in acute myeloid leukemia. *J. Clin. Invest.* **132**, e159579 (2022).
25. Mazziotta, F. et al. CD8+ T-cell differentiation and dysfunction inform treatment response in acute myeloid leukaemia. *Blood* **144**, 1168–1182 (2024).
26. Good, C. R. et al. An NK-like CAR T cell transition in CAR T cell dysfunction. *Cell* **184**, 6081–6100.e6026 (2021).
27. Penter, L. & Wu, C. J. Therapy response in AML: a tale of two T cells. *Blood* **144**, 1134–1136 (2024).
28. Döhner, H. et al. Diagnosis and management of AML in adults: 2017 ELN recommendations from an international expert panel. *Blood* **129**, 424–447 (2017).
29. Schmid, C. et al. Donor lymphocyte infusion in the treatment of first hematological relapse after allogeneic stem-cell transplantation in adults with acute myeloid leukemia: a retrospective risk factors analysis and comparison with other strategies by the EBMT Acute Leukemia Working Party. *J. Clin. Oncol.* **25**, 4938–4945 (2007).
30. Berger, C. et al. Adoptive transfer of effector CD8+ T cells derived from central memory cells establishes persistent T cell memory in primates. *J. Clin. Invest.* **118**, 294–305 (2008).
31. Schmidt, F. et al. In-depth analysis of human virus-specific CD8(+) T cells delineates unique phenotypic signatures for T cell specificity prediction. *Cell Rep.* **42**, 113250 (2023).
32. Quintelier, K. et al. Analyzing high-dimensional cytometry data using FlowSOM. *Nat. Protoc.* **16**, 3775–3801 (2021).
33. Larbi, A. & Fulop, T. From “truly naïve” to “exhausted senescent” T cells: When markers predict functionality. *Cytom. Part A* **85**, 25–35 (2014).
34. Gattinoni, L., Speiser, D. E., Lichterfeld, M. & Bonini, C. T memory stem cells in health and disease. *Nat. Med.* **23**, 18–27 (2017).
35. Wherry, E. J. & Kurachi, M. Molecular and cellular insights into T cell exhaustion. *Nat. Rev. Immunol.* **15**, 486–499 (2015).
36. Louie, R. H. Y. et al. CAR(+) and CAR(-) T cells share a differentiation trajectory into an NK-like subset after CD19 CAR T cell infusion in patients with B cell malignancies. *Nat. Commun.* **14**, 7767 (2023).
37. Andreatta, M., Berenstein, A. J. & Carmona, S. J. scGate: marker-based purification of cell types from heterogeneous single-cell RNA-seq datasets. *Bioinforma. (Oxf., Engl.)* **38**, 2642–2644 (2022).
38. Szabo, P. A. et al. Single-cell transcriptomics of human T cells reveals tissue and activation signatures in health and disease. *Nat. Commun.* **10**, 4706–4706 (2019).
39. Koh, J.-Y. et al. Identification of a distinct NK-like hepatic T-cell population activated by NKG2C in a TCR-independent manner. *J. Hepatol.* **77**, 1059–1070 (2022).
40. Good, Z. et al. Post-infusion CAR TReg cells identify patients resistant to CD19-CAR therapy. *Nat. Med.* **28**, 1860–1871 (2022).
41. Zheng, L. et al. Pan-cancer single-cell landscape of tumor-infiltrating T cells. *Science (New York, N.Y.)* **374**, abe6474–abe6474 (2021).
42. Daniel, B. et al. Divergent clonal differentiation trajectories of T cell exhaustion. *Nat. Immunol.* **23**, 1614–1627 (2022).
43. Giles, J. R. et al. Shared and distinct biological circuits in effector, memory and exhausted CD8+ T cells revealed by temporal single-cell transcriptomics and epigenetics. *Nat. Immunol.* **23**, 1600–1613 (2022).
44. Dominguez, C. X. et al. The transcription factors ZEB2 and T-bet cooperate to program cytotoxic T cell terminal differentiation in response to LCMV viral infection. *J. Exp. Med.* **212**, 2041–2056 (2015).
45. Trapnell, C. et al. The dynamics and regulators of cell fate decisions are revealed by pseudotemporal ordering of single cells. *Nat. Biotechnol.* **32**, 381–386 (2014).
46. Bergen, V., Lange, M., Peidli, S., Wolf, F. A. & Theis, F. J. Generalizing RNA velocity to transient cell states through dynamical modeling. *Nat. Biotechnol.* **38**, 1408–1414 (2020).
47. Cai, C. et al. Identification of human progenitors of exhausted CD8(+) T cells associated with elevated IFN-gamma response in early phase of viral infection. *Nat. Commun.* **13**, 7543 (2022).
48. Hensel, N. et al. Memory-like HCV-specific CD8(+) T cells retain a molecular scar after cure of chronic HCV infection. *Nat. Immunol.* **22**, 229–239 (2021).
49. Lahman, M. C. et al. Targeting an alternate Wilms’ tumor antigen 1 peptide bypasses immunoproteasome dependency. *Science Transl. Med.* **14**, eabg8070–eabg8070 (2022).
50. Abbas, H. A. et al. Single cell T cell landscape and T cell receptor repertoire profiling of AML in context of PD-1 blockade therapy. *Nat. Commun.* **12**, 6071–6071 (2021).
51. Dufva, O. et al. Immunogenomic Landscape of Hematological Malignancies. *Cancer cell* **38**, 424–428 (2020).
52. Lasry, A. et al. An inflammatory state remodels the immune microenvironment and improves risk stratification in acute myeloid leukemia. *Nat. Cancer* **4**, 27–42 (2023).
53. Schalck, A. et al. Single-Cell Sequencing Reveals Trajectory of Tumor-Infiltrating Lymphocyte States in Pancreatic Cancer. *Cancer Discov.* **12**, 2330–2349 (2022).
54. Zhang, C. et al. A single-cell analysis reveals tumor heterogeneity and immune environment of acral melanoma. *Nat. Commun.* **13**, 7250 (2022).
55. Wu, F. et al. Single-cell profiling of tumor heterogeneity and the microenvironment in advanced non-small cell lung cancer. *Nat. Commun.* **12**, 2540 (2021).
56. Craddock, C. et al. Clinical activity of azacitidine in patients who relapse after allogeneic stem cell transplantation for acute myeloid leukemia. *Haematologica* **101**, 879–883 (2016).
57. Wherry, E. J. et al. Lineage relationship and protective immunity of memory CD8 T cell subsets. *Nat. Immunol.* **4**, 225–234 (2003).
58. Jackson, S. E., Sedikides, G. X., Okecha, G. & Wills, M. R. Generation, maintenance and tissue distribution of T cell responses to human cytomegalovirus in lytic and latent infection. *Med Microbiol Immunol.* **208**, 375–389 (2019).
59. Pociupany, M., Snoeck, R., Dierickx, D. & Andrei, G. Treatment of Epstein-Barr Virus infection in immunocompromised patients. *Biochem Pharm.* **225**, 116270 (2024).
60. Appay, V. et al. Memory CD8+ T cells vary in differentiation phenotype in different persistent virus infections. *Nat. Med.* **8**, 379–385 (2002).
61. Newell, E. W. et al. Combinatorial tetramer staining and mass cytometry analysis facilitate T-cell epitope mapping and characterization. *Nat. Biotechnol.* **31**, 623–629 (2013).
62. Catalina, M. D., Sullivan, J. L., Brody, R. M. & Luzuriaga, K. Phenotypic and functional heterogeneity of EBV epitope-specific CD8+ T cells. *J. Immunol.* **168**, 4184–4191 (2002).
63. Callan, M. F. et al. CD8(+) T-cell selection, function, and death in the primary immune response in vivo. *J. Clin. Invest.* **106**, 1251–1261 (2000).
64. Abbott, R. J. et al. Asymptomatic primary infection with Epstein-Barr virus: observations on young adult cases. *J. Virol.* **91**, e00382–17 (2017).
65. Young, L. S. & Rickinson, A. B. Epstein-Barr virus: 40 years on. *Nat. Rev. Cancer* **4**, 757–768 (2004).
66. Sinzger, C. et al. Fibroblasts, epithelial cells, endothelial cells and smooth muscle cells are major targets of human cytomegalovirus infection in lung and gastrointestinal tissues. *J. Gen. Virol.* **76**, 741–750 (1995).

67. Nakamura, K. & Smyth, M. J. Myeloid immunosuppression and immune checkpoints in the tumor microenvironment. *Cell Mol. Immunol.* **17**, 1–12 (2020).
68. Muroyama, Y. & Wherry, E. J. Memory T-Cell Heterogeneity and Terminology. *Cold Spring Harbor Perspectives in Biology* **13**, a037929–a037929 (2021).
69. Miller, B. C. et al. Subsets of exhausted CD8+ T cells differentially mediate tumor control and respond to checkpoint blockade. *Nat. Immunol.* **20**, 326–336 (2019).
70. Zeidner, J. F. et al. Phase II Trial of Pembrolizumab after High-Dose Cytarabine in Relapsed/Refractory Acute Myeloid Leukemia. *Blood Cancer Discov.* **2**, 616–629 (2021).
71. Desai, P. N. et al. Single-Cell Profiling of CD8+ T Cells in Acute Myeloid Leukemia Reveals a Continuous Spectrum of Differentiation and Clonal Hyperexpansion. *Cancer Immunol. Res* **11**, 1011–1028 (2023). OF1-OF18.
72. Bhagwat, A. S. et al. Cytokine-mediated CAR T therapy resistance in AML. *Nat. Med.* **30**, 3697–3708 (2024).
73. Schuh, A. C. et al. Azacitidine in adult patients with acute myeloid leukemia. *Crit. Rev. Oncol. Hematol.* **116**, 159–177 (2017).
74. Apostolova, P. et al. Phase II trial of hypomethylating agent combined with nivolumab for acute myeloid leukaemia relapse after allogeneic haematopoietic cell transplantation-Immune signature correlates with response. *Br. J. Haematol.* **203**, 264–281 (2023).
75. Costantini, B. et al. The effects of 5-azacytidine on the function and number of regulatory T cells and T-effectors in myelodysplastic syndrome. *Haematologica* **98**, 1196–1205 (2013).
76. El Khawanky, N. et al. Demethylating therapy increases anti-CD123 CAR T cell cytotoxicity against acute myeloid leukemia. *Nat. Commun.* **12**, 6436 (2021).
77. Goodyear, O. et al. Induction of a CD8+ T-cell response to the MAGE cancer testis antigen by combined treatment with azacitidine and sodium valproate in patients with acute myeloid leukemia and myelodysplasia. *Blood* **116**, 1908–1918 (2010).
78. Amini, L. et al. Preparing for CAR T cell therapy: patient selection, bridging therapies and lymphodepletion. *Nat. Rev. Clin. Oncol.* **19**, 342–355 (2022).
79. Hahne, F. et al. flowCore: a Bioconductor package for high throughput flow cytometry. *BMC Bioinforma.* **10**, 106–106 (2009).
80. Nowicka, M. et al. CyTOF workflow: differential discovery in high-throughput high-dimensional cytometry datasets. *F1000Research* **6**, 748–748 (2017).
81. Lun, A. T. L. et al. EmptyDrops: distinguishing cells from empty droplets in droplet-based single-cell RNA sequencing data. *Genome Biol.* **20**, 63–63 (2019).
82. Dobin, A. et al. STAR: ultrafast universal RNA-seq aligner. *Bioinformatics* **29**, 15–21 (2013).
83. Amezquita, R. A. et al. Orchestrating single-cell analysis with Bioconductor. *Nat. methods* **17**, 137–145 (2020).
84. Bais, A. S. & Kostka, D. scds: computational annotation of doublets in single-cell RNA sequencing data. *Bioinforma. (Oxf., Engl.)* **36**, 1150–1158 (2020).
85. McCarthy, D. J., Campbell, K. R., Lun, A. T. L. & Wills, Q. F. Scater: pre-processing, quality control, normalization and visualization of single-cell RNA-seq. *data R. Bioinforma. (Oxf., Engl.)* **33**, 1179–1186 (2017).
86. Stuart, T. et al. Comprehensive Integration of Single-Cell Data. *Cell* **177**, 1888–1902.e1821 (2019).
87. Butler, A., Hoffman, P., Smibert, P., Papalexi, E. & Satija, R. Integrating single-cell transcriptomic data across different conditions, technologies, and species. *Nat. Biotechnol.* **36**, 411–420 (2018).
88. Gu, Z., Eils, R. & Schlesner, M. Complex heatmaps reveal patterns and correlations in multidimensional genomic data. *Bioinformatics* **32**, 2847–2849 (2016).
89. Andreatta, M. et al. Interpretation of T cell states from single-cell transcriptomics data using reference atlases. *Nat. Commun.* **12**, 2965–2965 (2021).
90. Wolf, F. A., Angerer, P. & Theis, F. J. SCANPY: large-scale single-cell gene expression data analysis. *Genome Biol.* **19**, 15–15 (2018).
91. Borcherdig, N., Bormann, N. L. & Kraus, G. scRepertoire: An R-based toolkit for single-cell immune receptor analysis. *F1000Research* **9**, 47–47 (2020).
92. Love, M. I., Huber, W. & Anders, S. Moderated estimation of fold change and dispersion for RNA-seq data with DESeq2. *Genome Biol.* **15**, 550–550 (2014).

Acknowledgements

We thank all members of the Chapuis and Greenberg lab for their contribution to the manuscript; the Fred Hutchinson Cancer Center Good Manufacturing Practice Cell Processing Facility for generating T_{TCR-C4}; the Immune Monitoring Laboratory for generating tetramers; the Flow Cytometry Facility for providing instruments and assistance in flow cytometry assays. We received funding from grant no. P01CA18029-41 (P.D.G.), grant no. NIH-5K08CA169485 (A.G.C.), NIH-T32CA080416 (M.C.L.), the Immunotherapy Integrated Research Center at the Fred Hutchinson Cancer Center (A.G.C., F.M.), Damon Runyon (A.G.C.), the Guillot Family ZachAttacksLeukemia Foundation (P.D.G.), Parker Institute for Cancer Immunotherapy (P.D.G.), Gabrielle’s Angel Foundation (A.G.C.), the V Foundation (A.G.C.). L.P. is a participant in the BIH Charité Digital Clinician Scientist Program funded by the DFG, the Charité – Universitätsmedizin Berlin, and the Berlin Institute of Health at Charité (BIH) and is supported by the Max-Eder program of the German Cancer Aid (Deutsche Krebshilfe), by the Else Kröner-Fresenius-Stiftung (2023_EKEA.102), the DKMS John Hansen Research Grant and the Brigitte und Dr. Konstanze Wegener-Stiftung (Project #133 A 2024 II (7)). Juno Therapeutics provided financial support for cell therapy product generation of this investigator-initiated trial. We thank all the patients who participated in this study.

Author contributions

Conception and design were performed by P.D.G., A.G.C., F.M. (Francesco Mazziotta), M.B., and T.M.S. Collection and assembly of data were carried out by F.M. (Francesco Mazziotta), L.E.M., A.G.C., K.G.P., D.N.E., M.B., N.D., V.V., P.L., D.H., B.L. Design, execution e/o analysis of in vitro experiments were performed by F.M. (Francesco Mazziotta), L.E.M., S.K., T.T. Data analysis and interpretation were performed by F.M. (Francesco Mazziotta), L.E.M., M.C.L., T.T., T.Z., V.V., R.G., C.C.S.Y., L.P., C.J.W., Y.A., E.C.W., F.M. (Filippo Milano), A.G.C., and P.D.G. All of the authors contributed to the writing of the manuscript. Final approval of the manuscript was given by all of the authors.

Competing interests

A.G.C. has received support from Juno Therapeutics, Lonza, and Affini-T. P.D.G. is a consultant, has received support from and has had ownership interest in Juno Therapeutics and Affini-T Therapeutics. He has also received support from Lonza, and consults and has ownership interest in Rapt Therapeutics, Elpiscience, Immunoscape, Earli, Metagenomi. Catalia, and Nextech. P.D.G., T.M.S., and the Fred Hutchinson Cancer Research Center have intellectual property related to TCR_{C4}. A.G.C. and K.G.P. have received reagents from 10X Genomics. R.G. has received consulting income from Takeda, Arcellx and Sanofi, and declares ownership in Ozette Technologies. CJW receives equity from BionTech, and is a SAB member of Repertoire, Adventris, Aethon Therapeutics and Nature’s Toolbox. M.B. is employed at Bristol Myers Squibb. The remaining authors declare no competing interests.

Additional information

Supplementary information The online version contains supplementary material available at (<https://doi.org/10.1038/s41467-025-60394-0>).

Correspondence and requests for materials should be addressed to Aude G. Chapuis.

Peer review information *Nature Communications* thanks the anonymous reviewer(s) for their contribution to the peer review of this work. A peer review file is available.

Reprints and permissions information is available at <http://www.nature.com/reprints>

Publisher's note Springer Nature remains neutral with regard to jurisdictional claims in published maps and institutional affiliations.

Open Access This article is licensed under a Creative Commons Attribution 4.0 International License, which permits use, sharing, adaptation, distribution and reproduction in any medium or format, as long as you give appropriate credit to the original author(s) and the source, provide a link to the Creative Commons licence, and indicate if changes were made. The images or other third party material in this article are included in the article's Creative Commons licence, unless indicated otherwise in a credit line to the material. If material is not included in the article's Creative Commons licence and your intended use is not permitted by statutory regulation or exceeds the permitted use, you will need to obtain permission directly from the copyright holder. To view a copy of this licence, visit <http://creativecommons.org/licenses/by/4.0/>.

© The Author(s) 2025

Francesco Mazziotta^{1,2,3}, Lauren E. Martin¹, Daniel N. Egan^{2,4,5}, Merav Bar^{2,4,6}, Sinéad Kinsella¹, Kelly G. Paulson^{2,4,5}, Valentin Voillet^{7,8}, Miranda C. Lahman¹, Daniel Hunter¹, Thomas M. Schmitt^{1,2}, Natalie Duerkopp^{1,2}, Cecilia C. S. Yeung^{2,9}, Tzu-Hao Tang¹, Raphael Gottardo^{10,11,12,13}, Yuta Asano¹, Elise C. Wilcox¹, Bo Lee¹, Tianzi Zhang¹, Paolo Lopedote¹⁴, Livius Penter^{15,16,17}, Catherine J. Wu¹⁵, Filippo Milano^{2,3}, Philip D. Greenberg^{1,2,18,19} & Aude G. Chapuis^{1,2,3,4,19} ✉

¹Program in Immunology, Fred Hutchinson Cancer Center, Seattle, WA, USA. ²Translational Sciences and Therapeutics Division, Fred Hutchinson Cancer Center, Seattle, WA, USA. ³Immunotherapy Integrated Research Center, Fred Hutch Cancer Center, Seattle, WA, USA. ⁴Division of Medical Oncology, University of Washington, Seattle, WA, USA. ⁵Providence-Swedish Cancer Institute, Seattle, WA, USA. ⁶Bristol Myers Squibb, Boudry, Switzerland. ⁷Vaccine and Infectious Disease Division, Fred Hutchinson Cancer Center, Seattle, WA, USA. ⁸Cape Town HVTN Immunology Laboratory, Hutchinson Centre Research Institute of South Africa, Cape Town, South Africa. ⁹University of Washington, Dept. of Laboratory Medicine and Pathology, Seattle, WA, USA. ¹⁰Biomedical Data Science Center, Lausanne University Hospital, Lausanne, Switzerland. ¹¹University of Lausanne, Lausanne, Switzerland. ¹²Agora Translational Research Center, Lausanne, Switzerland. ¹³Swiss Institute of Bioinformatics, Lausanne, Switzerland. ¹⁴Department of Medicine, St. Elizabeth's Medical Center, Boston University, Boston, MA, USA. ¹⁵Department of Medical Oncology, Dana-Farber Cancer Institute, Boston, MA, USA. ¹⁶Department of Hematology, Oncology, and Tumorimmunology, Campus Virchow Klinikum, Charité - Universitätsmedizin Berlin, Corporate Member of Freie Universität Berlin and Humboldt-Universität zu Berlin, Berlin, Germany. ¹⁷Berlin Institute of Health at Charité-Universitätsmedizin Berlin, BIH Biomedical Innovation Academy, BIH Charité Digital Clinician Scientist Program, Berlin, Germany. ¹⁸Departments of Immunology and Medicine, University of Washington, Seattle, WA, USA. ¹⁹These authors jointly supervised this work: Philip D. Greenberg, Aude G. Chapuis. ✉ e-mail: achapuis@fredhutch.org